

1 **Partial melting and strain localization in metapelites at very low-pressure conditions: the**  
2 **northern Apennines magmatic arc on the Island of Elba, Italy**

3 Samuele PAPESCHI<sup>a\*</sup>, Giovanni MUSUMECI<sup>a</sup>, Hans-Joachim MASSONNE<sup>b,c</sup>, Omar  
4 BARTOLI<sup>d</sup> and Bernardo CESARE<sup>d</sup>

5 a. Dipartimento di Scienze della Terra, Pisa University, via Santa Maria 53, 56126 Pisa, Italy

6 b. School of Earth Sciences, China University of Geosciences, 388 Lumo Road, 430074 Wuhan,  
7 P.R. China

8 c. Fakultät Chemie, Universität Stuttgart, Pfaffenwaldring 55, D-70569 Stuttgart, Germany

9 d. Dipartimento di Geoscienze, Padova University, via Giovanni Gradenigo 6, 35131 Padova,  
10 Italy

11

12 **\*Corresponding author:**

13 Primary e-mail: [s.papeschi@gmail.com](mailto:s.papeschi@gmail.com)

14 Institutional e-mail: [samuele.papeschi@unifi.it](mailto:samuele.papeschi@unifi.it)

15 Phone: +393202472057

16 Address: Dipartimento di Scienze della Terra, via Santa Maria 53, 56126 Pisa (PI), Italy.

17

18 **Authors' details**

19 **Samuele Papeschi**; [samuele.papeschi@unifi.it](mailto:samuele.papeschi@unifi.it) **ORCID**0000-0002-5774-7119

20 **Giovanni Musumeci**; [giovanni.musumeci@unipi.it](mailto:giovanni.musumeci@unipi.it) **ORCID**0000-0001-5343-4708

21 **Hans-Joachim Massonne**; [h-j.massonne@mineralogie.uni-stuttgart.de](mailto:h-j.massonne@mineralogie.uni-stuttgart.de) **ORCID**0000-0002-2826-  
22 4767

23 **Omar Bartoli**; [omar.bartoli@unipd.it](mailto:omar.bartoli@unipd.it)

24 **Bernardo Cesare**; [bernardo.cesare@unipd.it](mailto:bernardo.cesare@unipd.it) **ORCID**0000-0002-2340-1611

25

26 **Keywords:** partial melting; migmatite; shear zone; strain localization; in-situ melting;  
27 pseudosections.

28

29 **Highlights:**

- 30 • K-feldspar + plagioclase patches record in-situ partial melting in the upper crust;
- 31 • Melting was caused by granite emplacement and occurred in the andalusite field;
- 32 • Deformation is distributed in the partially molten rocks;
- 33 • Melt crystallization causes strain localization into mylonitic shear zones;
- 34 • First record of Alpine migmatite in the northern Apennines;

35 **Abstract**

36 Structural and microstructural analyses and phase equilibrium modeling of migmatitic amphibolite-  
37 facies metapelites from the late Carboniferous Calamita Schists, on the Island of Elba, Italy,  
38 show how the interplay between partial melting and regional (far-field) deformation assisted  
39 deformation at very shallow ( $P \leq 0.2$  GPa) crustal levels. Partial melting was caused by the heat  
40 supplied by an underlying late Miocene intrusion (Porto Azzurro pluton) and occurred by biotite  
41 continuous melting. The produced melt remained in situ in patches, likely experienced limited  
42 migration in stromatic migmatites, and crystallized as a K-feldspar + plagioclase + quartz  
43 assemblage. Deformation in the presence of melt occurred by melt-enhanced grain boundary  
44 sliding, producing well-foliated high-strain zones with weak evidence of subsolidus deformation  
45 at the microscale where the original melt was present. Melt crystallization caused strain  
46 hardening and forced subsolidus deformation into localized mylonitic shear zones. The localized  
47 character of retrograde deformation was likely determined by the heterogeneous  
48 distribution/ingress of fluids in the aureole that locally assisted strain localization, enhancing  
49 dislocation creep and reaction softening. Thus, this work documents the first occurrence of  
50 Alpine migmatites in the northern Apennines.

51

52 **1. Introduction**

53 Partial melting is commonly regarded as an effective weakening mechanism controlling strain  
54 localization in shear zones (Hollister and Crawford, 1986; Karlstrom et al., 1993; Davidson et  
55 al., 1994; Vanderhaeghe, 2009; Kruckenberg et al., 2011). Experimental results have shown that  
56 for very low melt fraction (between 1 and 4 vol%) the dominant deformation mechanism in  
57 rocks switches from dislocation creep to melt-enhanced grain boundary sliding, in

58 which interstitial melt allows grains to slide past each other (Cooper and Kohlstedt, 1984;  
59 Dell'Angelo et al., 1987; Dell'Angelo and Tullis, 1988; Walte et al., 2005; Zavada et al., 2007;  
60 Schulmann et al., 2008). At a higher melt fraction (~ 7-8 vol.%), melt becomes interconnected  
61 causing a further decrease in rock strength (the so called 'liquid percolation threshold' of  
62 Vigneresse and Tikoff, 1999 or the 'melt connectivity transition' of Rosenberg and Handy,  
63 2005). Deformation in the presence of a very low melt fraction (< 7%) not only causes strain  
64 partitioning between leucosomes and the residual rocks but also activates a positive feedback  
65 mechanism attracting more melt into high-strain zones, due to the local movements of grains  
66 (Rosenberg, 2001; Walte et al., 2005; Stuart et al., 2018).

67 The weakening effect of partial melting and melt migration in crustal and mantle rocks has been  
68 widely investigated (Rutter and Neumann, 1995; Vigneresse et al., 1996; Vigneresse and Tikoff,  
69 1999; Rosenberg and Handy, 2005; Misra et al., 2014), but the effect of in-situ crystallization of  
70 melt in migmatites has been broadly neglected. This is because the long-term rheology of  
71 migmatite terranes appears controlled by the efficiency of melt segregation and migration away  
72 from the residuum, causing strain hardening of the dry residual rocks (White and Powell, 2002;  
73 Brown, 2002, 2010; Guernina and Sawyer, 2003; Yakymchuck and Brown, 2014; Diener and  
74 Fagereng, 2014). However, solidification of melt has a significant impact on the rheology of  
75 melt-bearing systems, as the liquid-filled porosities are often pseudomorphosed by rheologically  
76 strong phases such as feldspars. For example, in syntectonic plutons the transition from syn-  
77 magmatic shearing to subsolidus deformation is often accompanied by extreme strain  
78 localization (e.g. Gapais, 1989; Pawley and Collins, 2002; Zibra et al., 2018). A similar  
79 transition in deformation and rheological behavior should be expected in high-strain zones in  
80 migmatites where melt crystallized in situ and did not segregate or where the presence of melt

81 was transient (for example in upper crustal aureoles; e.g. Pattison and Harte, 1988; Marchildon  
82 and Brown, 2002; Johnson et al., 2003; Droop and Brodie, 2012). Stuart et al. (2018)  
83 documented the preservation of pseudomorphs after melt-filled pores in granulitic rocks that  
84 were not overprinted by subsolidus deformation due to sudden increase in rock strength caused  
85 by melt crystallization. Localization of deformation in the subsolidus regime requires the  
86 activation of softening mechanisms which may cause strain partitioning between the leucosome  
87 and the residuum and drive strain localization (e.g. Diener et al., 2016; Miranda and Klepeis,  
88 2016; Stuart et al., 2018). Structures formed in the subsolidus range may be strikingly different  
89 in deformation style with respect to those formed in the presence of melt, reflecting the abrupt  
90 change in deformation mechanism and bulk rheology that follows melt solidification.

91 In this study, we investigated the structures recorded during transition from melt-present upper  
92 amphibolite-facies deformation to greenschist-facies mylonitization in the metasedimentary  
93 sequence of the Calamita Schists (northern Apennines, Island of Elba, Italy), within a  
94 synkinematic contact aureole developed at shallow crustal levels ( $P < 0.2$  GPa). We show an  
95 example where partial melting assisted large-scale deformation in high-strain domains. At  
96 decreasing temperature, melt crystallization caused strain hardening, as melt-enhanced  
97 deformation was deactivated. The localization of deformation during retrograde deformation was  
98 locally assisted by strain softening mechanisms leading to very heterogeneous distribution of  
99 strain marked by narrow and anastomosing shear zones that overprint the high-grade foliation.

100

## 101 **2. Geological Outline**

### 102 **2.1 Geology of the Island of Elba**

103 The Island of Elbais characterized by a stack of east-verging thrust nappes that was structured  
104 between the early Miocene and the Pliocene during the development of the Northern Apennines  
105 fold-and-thrust belt (Keller and Coward, 1996; Massa et al., 2017). The nappe stack is divided  
106 into an Upper Complex, which comprises non-metamorphic to lower greenschist-facies units and  
107 a Lower Complex consisting of the medium- to high-grade metamorphic Ortano and Calamita  
108 Units (Fig. 1a). The contact between the Upper and Lower Complexes is marked by the late  
109 Miocene out-of-sequence Capo Norsi – Monte Arco Thrust (Fig. 1a) that was active up to the  
110 early Pliocene (Tab. 1; Viola et al., 2018). The nappe stack is intruded by several late Miocene  
111 intrusives, notably the Monte Capanne pluton and the Central Elba laccolith complex, emplaced  
112 in the Upper Complex, and the Porto Azzurro pluton, intruded in the Calamita Unit and buried  
113 below the present-day sea level (Fig. 1a; Barberi et al., 1967; Dini et al., 2002; Musumeci and  
114 Vaselli, 2012; Barboni et al., 2015).

115 The Calamita Unit was deeply affected by the late Miocene low-pressure/high-temperature  
116 (LP/HT) metamorphic imprint caused by the emplacement of the Porto Azzurro pluton, which  
117 occurred at temperatures between 600 – 650 °C and pressures below 0.2 GPa (Duranti et al.,  
118 1992; Musumeci and Vaselli, 2012; Caggianelli et al., 2018). Pluton emplacement and LP/HT  
119 metamorphism were coeval with late Miocene contractional tectonics, which determined the  
120 development of ductile syn-magmatic shear zones, which were later overprinted by brittle, post-  
121 magmatic thrust sheets at the end of the thermal pulse (e.g. Capo-Norsi Monte Arco thrust in Fig.  
122 1a; Musumeci and Vaselli, 2012; Musumeci et al., 2015; Viola et al., 2018). LP/HT  
123 metamorphism and ductile deformation in the Calamita Unit were constrained between  
124  $6.76 \pm 0.08$  Ma ( $^{40}\text{Ar}/^{39}\text{Ar}$  phlogopite age) and  $6.23 \pm 0.06$  Ma ( $^{40}\text{Ar}/^{39}\text{Ar}$  muscovite age) (Tab. 1).  
125 A zirconimiyielded a  $6.40 \pm 0.15$  Ma U/Pb age (see Musumeci et al., 2015). The brittle overprint

126 was dated through  $^{40}\text{K}/^{40}\text{Ar}$  on authigenic illite between  $6.14\pm 0.64$  Ma and  $4.90\pm 0.27$  Ma (Tab.  
127 1; Viola et al., 2018). As a consequence, ductile deformation in the Calamita Unit, triggered by  
128 the thermal anomaly, very likely lasted less than 1 Ma.

129

## 130 **2.2 Strain and metamorphic gradients in the Calamita Unit**

131 The Calamita Unit (Fig.1a, b) is a metamorphic complex characterized by the early  
132 Carboniferous Calamita Schists, which are tectonically overlain by Triassic metaclastics  
133 (Barabarca quartzite), marbles and dolomitic marbles (Calanchiole marble; Barberi et al., 1967;  
134 Musumeci et al., 2011; Papeschi et al., 2017 and references therein). The Calamita Schists  
135 experienced LP/HT late Miocene amphibolite-facies metamorphism with peak temperatures  
136 around  $625\text{ }^{\circ}\text{C}$  (Caggianelli et al., 2018) or even exceeding  $650\text{ }^{\circ}\text{C}$  (Musumeci and Vaselli,  
137 2012) and were overprinted by greenschist-facies retrograde metamorphism during cooling of  
138 the Porto Azzurro pluton.

139 The metamorphic foliation in the Calamita Schists strikes N-S to NW-SE and dips generally to  
140 the W-SW. The Ripalte antiform (Fig. 1b) refolded the main metamorphic foliation, which  
141 became E-NE dipping to (locally) subvertical in the eastern part of the Calamita Unit. The  
142 antiform is interpreted as a late thrust fault-propagation fold that affected the Calamita Unit after  
143 the LP/HT metamorphic event (see Mazzarini et al., 2011 and Papeschi et al., 2017). Stretching  
144 lineations trend E-W and dip to the W and the E on the opposite limbs of the antiform (Fig. 1b).

145 The Calamita Schists consist of interlayered dark grey to brownish micaschists, metapsammites,  
146 and quartzites containing centimeter- to decimeter-thick deformed quartz layers: the  
147 compositional variability is largely due to varying quartz and mica content within the schists.  
148 Late Miocene contractional deformation is very heterogeneously distributed in the Calamita

149 Schists, which are characterized by well-foliated high-strain domains (Fig. 2a) with local  
150 mylonitic layers and top-to-the-E kinematic indicators, localized in low-strain domains that  
151 constitute the majority of the Calamita Schists (see in detail Papeschi et al., 2017). High-strain  
152 domains display a composite fabric that preserve relic upper amphibolite-facies deformation,  
153 highlighted by grain boundary migration in quartz, overprinted by lower amphibolite- to  
154 greenschist-facies mylonitic deformation and later brittle thrusting (Papeschi et al., 2018). In the  
155 eastern part of the Calamita Unit, high-strain domains are also affected by the Ripalte antiform,  
156 becoming locally E-dipping (Fig. 1b), apparently resembling normal shear zones. Low-strain  
157 domains are characterized by poorly foliated schists and hornfelses interlayered with quartz  
158 layers, that are locally affected by E-verging tight folds (Fig. 2b).

159 The metamorphic LP/HT assemblage of the Calamita Schists is characterized by white mica +  
160 biotite + cordierite + andalusite, overprinted by retrograde white mica and chlorite (see in detail  
161 Papeschi et al., 2017). The highest grade rocks of the Calamita Schists are located along the  
162 southeastern coast of the Calamita peninsula, in the core of the Ripalte antiform (Fig. 1b;  
163 Mazzarini et al., 2011; Papeschi et al., 2017), where they display the typical peak assemblage  
164 biotite + K-feldspar + plagioclase + andalusite + cordierite (first recognized by Barberi et al.,  
165 1967).

166

### 167 **3. Methodology**

168 In the present study we describe in detail two selected areas in the highest metamorphic grade  
169 portion of the Calamita Schists, showing the peak metamorphic assemblage (biotite + K-feldspar  
170 + plagioclase + andalusite + cordierite) with evidence of partial melting and its relationship with  
171 deformational structures: Punta Bianca and Capo Calvo (Fig. 1b). Several samples,



172 representative of the different structures and compositional domains identified in the field, were  
173 selected and analyzed in oriented thin sections (i.e. cut parallel to the lineation and perpendicular  
174 to the foliation). Details of the samples are available in the supplementary material to this article  
175 (Tab. S6) and on SESAR (<https://app.geosamples.org/>). Sample nomenclature strictly follows  
176 that of the SESAR database.

177 The petrographic microscope was used to identify mineral phases in a suite of samples,  
178 characterize microstructures, and select areas for investigations with a scanning electron  
179 microscope (SEM) and an electron microprobe (EMP). The area % of the phases present in  
180 selected samples (i.e. IESP3CS42A and IESP3SP196, see below) was estimated on thin section  
181 scans using the Color Threshold tool of the ImageJ software (Schneider et al., 2012),

182 Preliminary microstructural investigations and mineral analyses were carried out with a Hitachi  
183 TM3030 Plus Tabletop Microscope SEM at the Department of Earth Sciences (University of  
184 Pisa) and a ZEISS-EVO SEM equipped with an Oxford Instruments EDS detector at the National  
185 Institute for Geophysics and Volcanology (Pisa, Italy).

186 Rock-forming minerals were analyzed in a single sample (IESP3CS42A) with a CAMECA  
187 SX100 EMP equipped with five spectrometers and an EDS system at the Institut für Mineralogie  
188 und Kristallchemie (Universität Stuttgart). Analytical conditions for spot analyses were 15 kV  
189 accelerating voltage, 15 nA beam current, 20s counting time on peak and background each, and 1  
190  $\mu\text{m}$  spot size. Standards were wollastonite (Si, Ca),  $\text{Al}_2\text{O}_3$  (Al),  $\text{Fe}_2\text{O}_3$  (Fe),  $\text{MnTiO}_3$  (Mn, Ti),  
191 albite (Na), orthoclase (K), olivine (Mg) and barite (Ba). Structural formulae of minerals were  
192 recalculated considering 14 oxygen equivalents for chlorite, 11 for white mica, 22 for biotite, 18  
193 for pinitized cordierite, 8 for feldspar, 5 for andalusite, 3 for ilmenite, 5 for titanite, and 4 for  
194 rutile. Biotite was classified using the classification scheme based on the siderophyllite –

195 eastonite – phlogopite – annite end-members after Deer et al. (1992). Concentration maps for  
196 major elements (Ca, Fe, Mn, Mg, Al and Na) were also produced by stepwise movements of the  
197 thin section under the electron beam; counting times per step were 100 ms.

198 The bulk rock chemistry of sample IESP3CS42A was determined by X-ray fluorescence  
199 spectroscopy (XRF) using the Panalytical PW2400 spectrometer at the Institut für Mineralogie  
200 und Kristallchemie in Stuttgart. Whole-rock analyses, expressed in wt%, were recalculated in  
201 mol% for phase equilibria modeling using THERMOCALC 3.33 (Powell and Holland, 1998; see  
202 details in section 5).

203

#### 204 **4. Structural and lithological features**

##### 205 **4.1 Punta Bianca**

206 The mesoscale structures exposed at Punta Bianca are developed in the biotite + K-feldspar +  
207 plagioclase + andalusite + cordierite zone of the Calamita Schists, according to Barberi et al.  
208 (1967). The foliation strikes N-S to NW-SE, gently dipping to the E (10 to 30°) and is defined by  
209 the preferred orientation of the mineral assemblage (Fig. 2c, d). Upright, open to tight folds with  
210 N-S trending axes locally refold the main foliation (Fig. 2c). The Calamita Schists at Punta  
211 Bianca display a compositional banding defined by light-colored quartz-feldspar-rich  
212 layers interlayered with dark-colored biotite-rich bands (Fig. 2c, d). Moreover, millimeter to  
213 centimeter-thick quartzite layers, widely diffused in the Calamita schist from high- to low-  
214 metamorphic grade lithologies, are oriented parallel to the compositional banding. The  
215 compositional banding generally follows mesoscale structures such as folds (Fig. 2c) and  
216 foliations (Fig. 2d). Light-colored domains are composed of K-feldspar, plagioclase, and quartz  
217 with variable content of biotite, andalusite, and cordierite, range in thickness from few

218 millimeters to some centimeters, and are laterally continuous for several tens of centimeters (Fig.  
219 2d, e). Dark-colored domains consist of biotite, andalusite, less commonly, cordierite and  
220 contain discrete layers and pockets (Fig. 2f) of K-feldspar, plagioclase, and quartz. Intermediate-  
221 colored domains, characterized by a conspicuous content of both light- and dark-colored phases,  
222 are also widely present.

223 The foliation is heterogeneously distributed at outcrop scale and appears more penetrative in  
224 domains characterized by a higher proportion of quartz, K-feldspar, and plagioclase (e.g. Fig. 2e)  
225 with respect to dark-colored domains, that typically show randomly-distributed cm-sized  
226 andalusite grains and lack a clearly defined foliation (Fig. 2f).

227

## 228 **4.2 Capo Calvo**

229 Capo Calvo exposes amphibolite-facies schists and metapsammities containing biotite, quartz,  
230 andalusite, cordierite, K-feldspar, and plagioclase (Fig. 3a). The dominant fabric is a N-S to NW-  
231 SE striking and E-dipping penetrative foliation (mean dip-direction/dip: N061°/31°; Fig. 3a),  
232 defined by the preferred orientation of the amphibolite-facies assemblage, which is crosscut by  
233 anastomosing E-verging shear-zones (mean dip-direction/dip: N062°/53°; Fig. 3a) with a  
234 greenschist-facies white mica + chlorite bearing assemblage (described in detail in Papeschi et  
235 al., 2018). The eastern dip of structures at Capo Calvo is due to their position on the eastern flank  
236 of the late Ripalte antiform, which refolded originally W-dipping thrust shear zones (Fig. 1b;  
237 Mazzarini et al., 2011; Papeschi et al., 2018). Stretching lineations trend SW-NE dipping to the  
238 ENE (Fig. 3a).

239 As in Punta Bianca, the distribution of compositional domains and deformational features is  
240 heterogeneous at outcrop scale (Fig. 3b, c). The Calamita Schists display (1) whitish, deformed

241 quartz-rich layers (Fig. 3b), (2) dark-colored domains (Fig. 3b, c), consisting of very  
242 poorly foliated and coarse-grained blackish nodules containing mostly biotite, cm-sized euhedral  
243 andalusite or cordierite with pockets of K-feldspar, plagioclase, and quartz, and (3) light-colored  
244 domains, consisting of foliated schists containing biotite, quartz, K-feldspar, plagioclase,  
245 cordierite, and, less commonly, andalusite (Fig. 3b). Unlike Punta Bianca, light-colored domains  
246 display a conspicuous proportion of biotite, cordierite and andalusite. As shown in Fig. 3b, the  
247 transition from light- to dark-colored domains is gradational and marked by a progressive  
248 increase in quartz-feldspathic content from the former to the latter, corresponding also to an  
249 increase in foliation intensity (see also Fig. 3c). Greenschist-facies shear zones tend to be  
250 concentrated in light-colored domains but affected also dark-colored domains (Fig. 3c).

251 K-feldspar and plagioclase form more-or-less elongated mm- to cm-sized patches that are  
252 heterogeneously distributed in the biotite-rich groundmass (highlighted in Fig. 3c).

253

## 254 **5. Microstructures**

### 255 **5.1 Punta Bianca**

#### 256 *Dark-colored domains*

257 Dark-colored domains are composed of biotite, andalusite, cordierite, K-feldspar, plagioclase,  
258 quartz, and ilmenite and contain accessory tourmaline, zircon, apatite and monazite. Some  
259 domains display andalusite as part of the peak assemblage, whereas others cordierite. Very few  
260 domains contain both andalusite and cordierite. Quartz layers are locally interlayered within  
261 dark-colored domains. The foliation is generally poorly developed and the microstructure  
262 appears dominated by abundant coarse-grained (100 – 500  $\mu\text{m}$ ) decussate biotite grains that  
263 surround very large ( $> 1 \text{ mm}$ ) euhedral andalusite porphyroblasts (Fig. 4a). K-feldspar,

264 plagioclase, and quartz are heterogeneously distributed in fine-grained polycrystalline patches  
265 with irregular shape (Fig. 4a). The intensity of foliation increases in layers characterized by a  
266 higher proportion of K-feldspar, plagioclase, and quartz (Fig. 4b). The foliation is outlined by both  
267 the preferred orientation of biotite grains and the compositional banding defined by subparallel  
268 biotite-rich and quartz-feldspar-rich bands (Fig. 4b). Well-formed and relatively coarse-grained  
269 porphyroblasts of K-feldspar and plagioclase are only sporadically present and are surrounded by  
270 a rim of interstitial K-feldspar, quartz, and rare plagioclase (Fig. S1a in supplementary material).  
271 In the vast majority of cases K-feldspar, plagioclase and quartz form polygonal, polycrystalline  
272 aggregates (grain size: 50 – 200  $\mu\text{m}$ ) containing iso-oriented to decussate biotite inclusions (Fig.  
273 4c).

274 Biotite grains included in quartz-feldspathic aggregates frequently display a strongly irregular,  
275 resorbed outline (insert in Fig. 4c). On the other hand, biotite in large biotite aggregates (Fig. 4a)  
276 and included in K-feldspar and plagioclase porphyroblasts (Fig. S1a in supplementary material)  
277 displays subhedral to euhedral shape. Quartz, K-feldspar, and plagioclase between biotite  
278 grains frequently form a polygonal groundmass (Fig. 4d, e) that contains grains with well-defined  
279 crystal faces and triple-point junctions (as the quartz grain in Fig. 4d), coexisting with strongly  
280 irregular, interstitial grains that surround smaller grains (e.g. K-feldspar in Fig. 4e). Fig. 4f shows  
281 an example of interstitial quartz (orange) characterized by cusped lobes interfingered between  
282 the neighboring grains, which display straight crystal faces or a rounded outline. Resorbed grains  
283 may display abundant ilmenite inclusions, which are less common in interstitial phases (Fig. 4f).

284

285 *Light-colored domains*

286 Light-colored domains consist predominantly of quartz, K-feldspar, and plagioclase with very  
287 limited biotite, andalusite, and cordierite. Accessories are zircon, apatite, tourmaline, and  
288 monazite. Sericite is present as a retrograde phase, overgrowing K-feldspar and plagioclase.

289 As shown in Fig. 5a and 5b, the microstructure of light-colored domains is well-foliated, owing  
290 to stretched quartz grains, elongated K-feldspar + plagioclase aggregates that are often replaced  
291 by sericite, and the preferred orientation of few biotite grains. Quartz shows large grains (100 –  
292 500  $\mu\text{m}$ ) that are surrounded by small ( $\sim 10 - 50 \mu\text{m}$ ) grains indicative of recrystallization by  
293 bulging and subgrain rotation (Fig. 5a). The large grains are characterized by amoeboid shape  
294 and lobate grain boundaries, indicative of grain boundary migration recrystallization (see Stipp et  
295 al., 2002).

296 K-feldspar and plagioclase are frequently organized in stretched layers that follow domains  
297 where few biotite grains are still preserved although strongly resorbed by cusped lobes of K-  
298 feldspar (Fig. 5c). In spite of the strong elongation of feldspar aggregates (e.g. Fig. 5b), K-  
299 feldspar and plagioclase display a polygonal microstructure made up of polycrystalline  
300 aggregates with 50 – 200  $\mu\text{m}$  average grain size that lacks extensive dynamic recrystallization  
301 features (Fig. 5d). Larger porphyroblasts (up to some hundreds of microns) are also present. In  
302 feldspar aggregates, euhedral grains of K-feldspar and plagioclase with well-developed crystal  
303 faces coexist with rounded K-feldspar, plagioclase, and quartz grains, surrounded by interstitial  
304 K-feldspar and/or quartz (Fig. 5d). Several cusped lobes of K-feldspar with low dihedral angles  
305 penetrate between adjacent quartz and K-feldspar grains are shown in Fig. 5d as an example.

306

## 307 **5.2 Capo Calvo**

308 *Dark-colored domains*

309 At Capo Calvo, dark-colored domains display similar features with respect to Punta Bianca, but  
310 they are overprinted by an intense retrograde metamorphism that produced fine-grained  
311 aggregates of sericite and chlorite over biotite, andalusite, cordierite, K-feldspar, and plagioclase  
312 (Fig. 6a). Accessories are tourmaline, zircon, apatite, and monazite. Quartz is present as  
313 deformed layers with amoeboid-shaped grains.

314 As shown in Fig. 6a, biotite is (partially) replaced by andalusite, cordierite, K-feldspar, and  
315 plagioclase. K-feldspar + plagioclase + quartz aggregates with 50 – 200  $\mu\text{m}$  grain size and  
316 polygonal texture occur scattered through the microstructure, surrounded by retrograde sericite  
317 (Fig. S1g in supplementary material). K-feldspar is commonly characterized by strongly cusped  
318 and irregular lobes that penetrate between quartz and biotite grain boundaries (Fig. 6b). We  
319 observed small feldspar grains included in quartz in optical continuity with larger grains (Fig.  
320 6b). Biotite, with strongly irregular and resorbed shape, is commonly surrounded by interstitial  
321 K-feldspar and /or quartz (Fig. 6c). The internal microstructure of K-feldspar, plagioclase, and  
322 quartz aggregates is generally characterized by a polygonal texture with euhedral grains and  
323 rounded grains that are spatially associated with interstitial K-feldspar and quartz (Fig. 6d).  
324 Interstitial grains with triangular outline, localized close to triple junctions of euhedral grains are  
325 diffuse (Fig. 6d and S1h in supplementary material).

326

### 327 *Light-colored domains*

328 The description of light-colored domains is focused on sample (IESP3CS42A on SESAR  
329 database) that was also investigated in detail for mineral chemistry and modeled with  
330 pseudosections (see section 7).

331 Sample IESP3CS42A is a schist consisting of quartz, biotite, K-feldspar, plagioclase, cordierite  
332 (pinitized), and ilmenite (in modal order; Fig. 7a), locally overprinted by retrograde sericite,  
333 chlorite, and greenish biotite. The light color of the schist is largely due to the relative high  
334 abundance of quartz and feldspars. Andalusite is very rare and was found only as a fractured  
335 porphyroblast strongly replaced by white mica (Fig. S8 in supplementary material). Accessories  
336 are apatite (grain size: 100-500  $\mu\text{m}$ ), tourmaline (50-100  $\mu\text{m}$ ), zircon, monazite (less than 50-80  
337  $\mu\text{m}$ ), and titanite (50-100  $\mu\text{m}$ ). As shown in Fig. 7a, the sample displays a foliated microfabric  
338 defined by parallel quartz- (thickness: 1-5 mm) and biotite-rich domains (thickness: 100  $\mu\text{m}$  up  
339 to 1-2 mm), together constituting 91 area% of the whole sample. The remaining 9% of the  
340 sample area is made up of K-feldspar and plagioclase (6%) and cordierite (~ 2.5%).

341 As shown in Fig. 7b, quartz is characterized by large grains (200 – 700  $\mu\text{m}$  grain size) with  
342 amoeboid shape and strongly lobate grain boundaries, showing dissection microstructures and  
343 ‘island grains’ (i.e. small grains in optical continuity with larger grains; see Urai et al., 1986).  
344 Quartz grain boundaries are often pinned or dragged around subparallel biotite inclusions  
345 (pinning microstructure; see Jessell, 1987), defining the foliation within quartz-rich domains  
346 (Fig. 7c). Quartz microstructures are consistent with recrystallization by grain boundary  
347 migration (see Stipp et al., 2002). Only locally, quartz grains show patchy to undulose extinction,  
348 indicating a lower temperature overprint. Biotite-rich domains display a lepidoblastic  
349 microstructure defined by coarse-grained (100 – 500  $\mu\text{m}$ ) subparallel biotite grains with  
350 subhedral habit and undulose extinction (Fig. 7c) and small (~10-50  $\mu\text{m}$ ) subparallel grains of  
351 ilmenite. Fig. 7a highlights that cordierite, K-feldspar, and plagioclase occur strictly associated  
352 with biotite-rich layers. Cordierite forms euhedral to subhedral porphyroblasts (grain size: 0.1 – 1



353 mm) that are completely pseudomorphosed by mixtures of phyllosilicates (i.e. pinites) still  
354 preserving equilibrium textures with the surrounding biotite-rich matrix (Fig. 7d).

355 K-feldspar and plagioclase occur as polycrystalline patches and augen-like aggregates that can be  
356 as large as some millimeters and are generally characterized by a grain size of  $\sim 100 - 500 \mu\text{m}$   
357 (Fig. 7e). These aggregates are strictly localized in biotite-rich layers. K-feldspar is modally more  
358 abundant than plagioclase. Locally, small anhedral grains of quartz are also part of the K-feldspar  
359 + plagioclase aggregates.

360 As shown in Fig. 8a, K-feldspar + plagioclase aggregates are characterized by an irregular  
361 outline with several cusped lobes protruding in the surrounding quartz and biotite (red  
362 arrows). Feldspar grains can display poikiloblastic texture due to abundant biotite inclusions. Thin  
363 ( $<50 \mu\text{m}$  in thickness), K-feldspar-rich layers are also localized within quartz, in correspondence  
364 of biotite-rich domains (green arrow in Fig. 8a). Biotite in contact with or included in K-feldspar  
365 shows a very irregular outline indicating replacement of biotite by K-feldspar and plagioclase  
366 (light blue arrow in Fig. 8a). A significant fraction of the smaller biotite grains included in K-  
367 feldspar and plagioclase (grain size:  $5 - 100 \mu\text{m}$ ) displays well developed crystal faces  
368 and anhedral habit and appears clearly misoriented with respect to the main foliation (insert in  
369 Fig. 8a).

370 The contact between K-feldspar and plagioclase aggregates and the surrounding phases is often  
371 characterized by cusped lobes of feldspars (predominantly K-feldspar) with a smooth outline  
372 that extends for several tens of micrometers (Fig. 8b, c). Fig. 8b shows the contact of the K-  
373 feldspar rich aggregate of Fig. 8a with the surrounding quartz. Several tiny protrusions of K-  
374 feldspar into quartz and small K-feldspar grains, included in quartz, are in optical continuity with  
375 larger grains. The smaller K-feldspar aggregate of Fig. 8c, localized at the contact between

376 biotite and quartz, displays a strongly irregular shape and is interfingered with the surrounding  
377 biotite and quartz grains. Biotite appears strongly resorbed displaying lobes of K-feldspar that  
378 penetrate biotite grains mainly along their cleavage planes (Fig. 8c). Quartz grains with either  
379 well-developed crystal faces or a rounded outline occur at the contact between K-feldspar and  
380 quartz (Fig. 8c). Lobes of K-feldspar with very low apparent dihedral angle penetrate between  
381 boundaries of quartz grains (Fig. 8c). Small films of K-feldspar (down to a thickness of 1-5  $\mu\text{m}$ )  
382 diffusely occur at the contact between quartz and biotite grains or between biotite grains (Fig.  
383 8d). The shape of K-feldspar and plagioclase grains ranges from euhedral to anhedral. As shown  
384 in Fig. 8e, many K-feldspar and plagioclase grains display sharp, planar contacts with well-  
385 developed crystal faces. Interstitial K-feldspar, plagioclase, and quartz surround euhedral to  
386 partially rounded K-feldspar and plagioclase grains (Fig. 8f).

387

### 388 *Transition to shear zones*

389 The transition from the light-colored/dark-colored domains to shear zones, corresponding to the  
390 transition from the foliated schists to the top-to-the-E shear zones shown in Fig. 3c, is marked by  
391 an increase in strain and a change in composition and metamorphic grade.

392 An example is shown in Fig. 9a, which highlights the contact between a quartz-biotite schist  
393 (wall rock) and a cm-thick top-to-the-E shear zone (sample IESP3SP196 on SESAR and in  
394 supplementary material, analyzed via ImageJ). The wallrock consists of amphibolite-facies  
395 subparallel quartz (~60 area %) and biotite  $\pm$  white mica (~25%) layers, defining a foliation  
396 obliquely oriented with respect to the shear zone boundary (dashed line in Fig. 9a), aggregates  
397 and porphyroclasts of K-feldspar and plagioclase (~13%), and cordierite porphyroclasts. White  
398 mica (incl. sericite) is present as retrograde phase locally overprinting K-feldspar, plagioclase,

399 and cordierite. The shear zone largely (~85%) consists of very fine-grained (< 10 µm)  
400 phyllosilicates (mostly sericite) with minor very fine-grained (< 5 – 20 µm grain size) quartz  
401 ribbons (~15%) defining a penetrative mylonitic foliation (subhorizontal in Fig. 9a), locally  
402 interrupted by E-verging C'-shear bands. For a detailed description of the shear-zone  
403 microfabric, the reader is referred to Papeschi et al. (2018).

404 The wall rock displays a foliated microstructure characterized by subparallel quartz- and biotite-  
405 rich layers (Fig. 9b). Biotite grains (grain size: 100 – 300 µm) feature undulose extinction and  
406 numerous kink bands (Fig. 9b). Quartz occurs as large grains (up to 1 mm) with lobate  
407 boundaries and amoeboid shape, indicative of grain boundary migration recrystallization (see  
408 Stipp et al., 2002), that are overprinted by undulose extinction and surrounded by small grains  
409 with serrated grain boundaries and subgrains, recrystallized by subgrain rotation and bulging  
410 recrystallization mechanisms (Fig. 9c).

411 Quartz and biotite surround porphyroclastic aggregates of K-feldspar + plagioclase,  
412 compositionally dominated by K-feldspar and ranging in size from some hundreds of microns to  
413 several millimeters (as in Fig. 9d). Locally, these feldspars form layers or lenses parallel to the  
414 foliation (Fig. 9a) and display a poikiloblastic microstructure due to abundant biotite and quartz  
415 inclusions (Fig. 9d). K-feldspar and plagioclase aggregates display strain caps, where quartz and  
416 biotite are dynamically recrystallized down to 10 – 80 µm, and strain shadows containing quartz,  
417 biotite, and white mica grains or even small sericite aggregates (Fig. 9e). Bookshelf sliding of K-  
418 feldspar and plagioclase, synthetic with the sense of shear, is diffuse.

419 The internal structure of K-feldspar and plagioclase aggregates is characterized by euhedral to  
420 subhedral grains (grain size: 50 to 1000 µm) with well-developed crystal faces (Fig. 10a, b).  
421 Interstitial grains, usually elongated films of K-feldspar and/or quartz, are interposed between

422 grains that in place show a linear or a rounded outline(Fig. 10a). ‘String of beads’  
423 microstructures(Holness et al., 2011) locally occur associated with interstitial grains. Phase  
424 boundaries within the aggregates vary from straight to lobate or serrated (Fig. 10b).  
425 K-feldspar and plagioclase are extensively recrystallized by subgrain rotation and bulging (grain  
426 size: 10 – 50  $\mu\text{m}$ ; Fig. 10c)in proximity with the shear zone boundary and occur as stretched  
427 ribbons displaying relatively large (100 - 200 $\mu\text{m}$ ) porphyroclasts surrounded by very fine-  
428 grained grains. Quartz layers interlayered with recrystallized feldspars generally display coarser  
429 grain size (100 – 500  $\mu\text{m}$ ). Feldspar ribbons are in part dynamically retrogressed to white  
430 mica/sericite, forming mixed feldspar/sericite layers as in the upper right corner of Fig. 10c), or  
431 extensively replaced by sericite-dominated ribbons with a grain size of 5-20  $\mu\text{m}$ , in which only  
432 few feldspar relics are recognizable (Fig. 10d).

433

## 434 **6. Evidence of partial melting in the Calamita Schists**

435 The Calamita Schists in Punta Bianca and Capo Calvo display the peak assemblage biotite +  
436 quartz + K-feldspar + plagioclase + ilmenite, with andalusite or cordierite (or both) depending on  
437 the protolith. Meso- and microstructural evidence (following Sawyer, 1999, 2008) suggests that  
438 the investigated rocks underwent partial melting, as we show in the following text.

439 We interpret the strongly replaced biotite and the K-feldspar, quartz, and plagioclase grains with  
440 rounded outline as residual phases (Fig. 4c, 6b, 8a)that were partially  
441 dissolved/consumedthrough melting reactions. The melt crystallized as K-feldspar + quartz +  
442 plagioclase, which are found as interstitial phases (e.g. Fig. 4f, 8d, 10a) and form cusped lobes  
443 with a strongly irregular outline against the residual phases (e.g. Fig. 6b, 8b, 8c). In particular,  
444 interstitial films of K-feldspar with very low apparent dihedral angle (e.g. Stuart et al., 2018) that

445 occur between biotite and quartz grains indicate crystallization within former melt-filled pores  
446 (Fig. 8d; see also Holness and Sawyer, 2008 for similar examples). Euhedral K-feldspar and  
447 plagioclase that have crystal faces against interstitial K-feldspar, plagioclase, and quartz are  
448 interpreted as early crystallization products of melt. These feldspars may have also in part grown  
449 from residual cores (e.g. Fig. 8c, 8e). Therefore, the K-feldspar + plagioclase + quartz  
450 aggregates can be interpreted as pools and patches of former melt that contain residual grains of  
451 previously-formed metamorphic feldspars and quartz (Fig. 7e). Similar microstructural criteria to  
452 identify former melt and reactant minerals are reported by Platten (1982), Pattison and Harte  
453 (1988), Holness and Clemens (1999), Sawyer (2008), and Holness et al. (2011). We exclude that  
454 the aforementioned microstructures indicating former presence of melt might be ascribed to  
455 injection of magma, as they are invariably found throughout the investigated rocks (i.e. they do  
456 not represent a local feature) and are organized in discontinuous, diffuse interstitial films and  
457 patches rather than in discrete bodies in sharp contact with the host rocks (e.g. Fig. 2f). The  
458 occurrence of injected melts is only testified by leucocratic aplitic or pegmatitic tourmaline-  
459 bearing dykes that crosscut the metamorphic foliation/banding (e.g. Fig. 2d).

460 There is a strict correlation between the presence of former patches of leucosome and the  
461 availability of reactant biotite because K-feldspar + plagioclase + quartz aggregates are often  
462 found localized in biotite-rich layers (e.g. Fig. 7a), where biotite is strongly resorbed (e.g. Fig.  
463 4c, 5c). Even in light-colored domains in Punta Bianca, where only few biotite layers are present,  
464 K-feldspar + plagioclase + quartz aggregates appear to follow reactant biotite-rich domains (e.g.  
465 Fig. 5c). These observations suggest that the elongated feldspar aggregates represent domains  
466 where all biotite reacted away, i.e. biotite layers are ‘fertile’ layers (Fig. 5b). Strongly resorbed  
467 biotite grains, consumed by partial melting, coexist with smaller and euhedral biotite grains that

468 are in equilibrium with K-feldspar (e.g. Fig 8a). Such grains may be interpreted either as  
469 crystallized from the melt (i.e. liquidus phase) or as product of an incongruent melting reaction  
470 (i.e. peritectic phase) (see e.g. Platten, 1982 and Sawyer, 2008). We exclude that these grains  
471 might have been passively included, because of the strong corrosion of biotite in rocks at both  
472 investigated localities. Cordierite and andalusite, which form euhedral porphyroblasts (e.g. Fig.  
473 4a, 8d), are suggested to be peritectic phases that were in equilibrium with the melt-bearing peak  
474 mineral assemblage, as also suggested by the strongly resorbed shape of biotite in contact with  
475 andalusite and cordierite (e.g. Fig. 6a).

476 The distribution of leucosomes at the micro- and meso-scale, largely organized in discrete  
477 patches (e.g. Fig. 5c) and interstitial films or pools, led us to classify the studied rocks as patch  
478 migmatites (according to Sawyer, 2008). Only in Punta Bianca, melt appears to have been  
479 organized in discrete layers (e.g. Fig. 2e) because we interpret the compositional layering  
480 between light-colored and dark-colored domains at this locality to be the result of the original  
481 abundance of melt in the different domains. In particular, the high K-feldspar + plagioclase  
482 content of light-colored domains together with their relative low content of biotite suggests that  
483 they were originally rich in melt as a result either of fertility or melt migration. Therefore, the  
484 banded rocks of Punta Bianca can be interpreted as stromatic migmatites (according to Sawyer,  
485 2008).

486

## 487 **7. Metamorphic Petrology**

488 Whole-rock and mineral chemistry was carried out on sample IESP3CS42A (Fig. 7, 8).  
489 This patch migmatite sample was chosen based on (1) the clear relationships between partial  
490 melting microstructures and the peak mineral assemblage (quartz + biotite + cordierite + K-

491 feldspar + plagioclase) and (2) the lack of structures indicating migration and partitioning of melt  
492 into discrete leucosomes. Thus, no significant melt loss after partial melting was inferred for  
493 sample IESP3CS42A.

494

## 495 **7.1 Mineral Chemistry**

496 Representative mineral analyses of sample IESP3CS42A are listed in Tab. 2. All analyses are  
497 provided in the supplementary material. K-feldspar displays a Na-poor composition ( $\text{Or}_{90-100}$ )  
498 whereas plagioclase shows an oligoclase composition ( $\text{An}_{10-17}$ ). Ilmenite is characterized by Mn  
499 contents between 0.05 and 0.12 per formula unit (p.f.u.) and  $\text{Fe}^{3+}$  contents  $< 0.01$  p.f.u (Tab. 2).  
500 Concentration maps were acquired on biotite grains (1) aligned along the foliation and  
501 containing interstitial K-feldspar (Fig. 11a) and (2) included in K-feldspar (Fig. 11b). Biotite  
502 grains show in general a homogeneous distribution of Fe, Mg, and Al (Fig. 11c, d, f, g) and a  
503 zoning characterized by an increase in Ti towards the rims (Fig. 11e, h). The compositional maps  
504 of Fig. 11c, d highlight the presence of thin laminae of K-feldspar, frequently altered to sericite,  
505 localized between biotite grains. Small rutile and chlorite grains occur as alteration phases (Fig.  
506 11d, e).

507 Resorbed biotite grains included in K-feldspar are characterized by lobes of K-feldspar that  
508 clearly interrupt the Ti-zoning pattern (Fig. 11h). As shown in Fig. 11f, g euhedral biotite grains  
509 included in K-feldspar are, on the other hand, compositionally homogeneous and lack any Ti-  
510 zoning pattern (Fig. 11h). Mineral analyses of biotite were distinguished based on their habit  
511 (resorbed vs euhedral). The  $X_{\text{Fe}}$  ( $=\text{Fe}/[\text{Fe} + \text{Mg}]$ ) values of biotite range between 0.6 and 0.7,  
512 with euhedral biotite characterized by slightly lower Al contents and  $X_{\text{Fe}}$  between 0.60 and 0.65  
513 (Fig. 12a). The Ti contents of euhedral biotite grains are between 0.2 and 0.3 p.f.u., comparable

514 to that of the cores of resorbed biotite grains. Higher Ti contents, between 0.3 and 0.5 p.f.u., were  
515 detected on the rim of resorbed biotite grains (Fig. 12b, Tab. 2). We noted an increased scatter  
516 towards lower  $X_{\text{Fe}}$  values in resorbed biotite rims that we interpret as alteration along grain  
517 boundaries (Fig. 12a, b). The investigated sample contains also greenish, retrograde biotite (Fig.  
518 S10 in supplementary material), which is characterized by low  $X_{\text{Fe}}$  values and Al contents and Ti  
519 contents between 0.10 and 0.15 p.f.u. (Fig. 12a, b). Pinitized cordierite displays a large  
520 variability in Mg, Fe, and Al contents, yet showing relatively constant  $X_{\text{Fe}}$  between 0.48 and  
521 0.58.

522

## 523 **7.2 Geothermometry**

524 Ti-in-biotite geothermometry was performed on sample IESP3CS42A applying the  
525 geothermometer calibrated by Wu and Chen (2015). This geothermometer was calibrated for the  
526 pressure-temperature (P-T) range of 450 – 840 °C and 0.1 – 1.9 GPa and, contrarily to the biotite  
527 geothermometer of Henry et al. (2005), is optimized for ilmenite- and/or rutile-bearing samples,  
528 making it suitable for the selected sample. Nevertheless, the geothermometer by Henry et al.  
529 (2005) was also applied to confront the results: temperature estimates resulting from the  
530 application of both geothermometers are available in the supplementary material.

531 For the calculation, all iron was considered to be divalent, based on the lack of  $\text{Fe}^{3+}$  bearing  
532 phases such as magnetite. The input pressure was set to 0.2 GPa (maximum metamorphic  
533 pressure for the Calamita Schists according to Musumeci and Vaselli, 2012). Temperature  
534 estimates on resorbed biotite grains range between 570 and 730 °C (average:  $629 \pm 57$  °C; Fig.  
535 12c) in biotite cores and 600 and 730 °C (average:  $654 \pm 36$  °C; Fig. 12c) in biotite rims, based  
536 on the geothermometer by Wu and Chen (2015). The application of the geothermometer by



537 Henry et al. (2005) yielded similar results yet providing systematically ~10 – 30 °C higher  
538 temperatures compared to those obtained with the geothermometer by Wu and Chen (2015).

539

### 540 **7.3 Phase equilibrium modeling**

541 The bulk composition of sample IESP3CS42A, expressed in wt% is: 72.52 SiO<sub>2</sub>, 0.67 TiO<sub>2</sub>,  
542 14.44 Al<sub>2</sub>O<sub>3</sub>, 4.07 Fe<sub>2</sub>O<sub>3</sub>, 0.05 MnO, 1.51 MgO, 0.50 CaO, 1.53 Na<sub>2</sub>O, 3.47 K<sub>2</sub>O, and 0.15 P<sub>2</sub>O<sub>5</sub>.

543 The bulk composition was recalculated as mol% to fit into the MnO – Na<sub>2</sub>O – CaO – K<sub>2</sub>O – FeO  
544 – MgO – Al<sub>2</sub>O<sub>3</sub> – SiO<sub>2</sub> – H<sub>2</sub>O – TiO<sub>2</sub> (MnNCKFMASHT) system, used for phase  
545 equilibrium modeling (Fig. 13). For this purpose, P<sub>2</sub>O<sub>5</sub> was fractionated as apatite, together with the  
546 corresponding amount of CaO. All Fe was considered as divalent, owing to the lack of Fe<sup>3+</sup>-rich  
547 oxides and the negligible amount of Fe<sup>3+</sup> in the analyzed minerals. Pseudosections were  
548 calculated using THERMOCALC 3.33 (Powell and Holland, 1988) and the internally consistent  
549 thermodynamic dataset ds55 by Holland and Powell (1998; updated November 2003). The  
550 following solid solution models were used: amphibole (Diener et al., 2007), silicate melt (White  
551 et al., 2007), cordierite, staurolite, chlorite (combination of Mahar et al., 1997 and Holland and  
552 Powell, 1998), garnet, biotite, ilmenite, hematite (White et al., 2005), orthopyroxene, spinel,  
553 magnetite (White et al., 2002), chloritoid (combination of Mahar et al., 1997 and White et al.,  
554 2000), muscovite, paragonite (Coggon and Holland, 2002), plagioclase, and K-feldspar (Holland  
555 and Powell, 2003). The fluid was considered to be pure H<sub>2</sub>O (X<sub>H<sub>2</sub>O</sub> = 1). The pseudosection  
556 shown in Fig. 13 was calculated assuming water-saturated conditions, as it commonly occurs in  
557 prograde metapelites in contact aureoles (e.g. Buick et al., 2004). The suprasolidus part of the  
558 pseudosection was calculated using a fixed H<sub>2</sub>O content of 1.66 mol%, calculated using the rbi  
559 script of THERMOCALC assuming 0.5 vol.% of water at the solidus at 0.2 GPa.

560 Sample IESP3CS42A is characterized by a muscovite-free assemblage at the metamorphic peak,  
561 indicating that this rock equilibrated at temperatures above the muscovite-out reaction. The peak  
562 assemblage cordierite + biotite + K-feldspar + plagioclase + ilmenite + quartz is stable between  
563 0.05 - 0.32 GPa and 530 – 710 °C in an esavariant field (Fig. 13). The calculated  $X_{\text{Fe}}$  isopleths  
564 for cordierite and biotite match the observed  $X_{\text{Fe}}$  on resorbed biotite (Fig. 12b) and, in part,  
565 pinitized cordierite. The composition of biotite within the cordierite + biotite + K-feldspar +  
566 plagioclase + ilmenite + quartz field becomes progressively poorer in iron towards higher  
567 temperatures, starting from  $X_{\text{Fe}} \sim 0.72$  at  $\sim 550$  °C to  $X_{\text{Fe}} \sim 0.66$  at  $\sim 650$  °C (Fig. 13). The same  
568 trend is observed in resorbed biotite grains which show a decrease in  $X_{\text{Fe}}$  from core to rim (Fig.  
569 12b), corresponding to a temperature range from 570 to 730 °C, based on Ti-in-biotite  
570 geothermometry (Fig. 12c). The biotite model of White et al. (2005), used for phase  
571 equilibriamodeling, estimates a Ti-content of biotite for the 570 – 730 °C temperature interval,  
572 which is significantly smaller ( $\sim 0.01$  to 0.1 p.f.u. on a 22 oxygen basis).

573 The wet solidus intersects the cordierite + biotite + K-feldspar + plagioclase + ilmenite + quartz  
574 field between 0.12 and 0.31 GPa at T between 656 and 713 °C (Fig. 13). At  $P < 0.12$  GPa, partial  
575 melting occurs in the presence of orthopyroxene and, at  $P > 0.31$  GPa, in the presence of  
576 sillimanite (Fig. 13). The peritectic biotite that is expected to persist in the presence of melt  
577 (cordierite + biotite + melt + plagioclase + ilmenite + quartz field) is characterized by  $X_{\text{Fe}} < 0.66$   
578 down to 0.62 (Fig. 13) matching the observed  $X_{\text{Fe}}$  of euhedral biotite ( $X_{\text{Fe}} = 0.60 - 0.65$ ; Fig.  
579 12a, b).

580

## 581 **8. Discussion**

### 582 **8.1 P-T conditions of partial melting in the Calamita Schists**

583 This study provides field and microstructural evidence (see sect. 5) of late Miocene partial  
584 melting in metapsammities from the high-strain domains of the Calamita Schists, in the southeast  
585 of the Island of Elba. We have demonstrated the presence of both stromatic migmatites (Punta  
586 Bianca), in which melt was concentrated in bands, and patch migmatites (Capo Calvo), in which  
587 leucosomes remained unsegregated. These anatexic rocks, formed in association with shallow  
588 intrusives in the Northern Tyrrhenian magmatic arc, are the unique example of crustal anatexis in  
589 the Northern Apennines. Phase equilibrium modeling (Fig. 13) constrains in-situ partial melting in  
590 the patch migmatite sample (IESP3CS42A) between 0.12 and 0.31 GPa for temperatures  
591 between 660 and 710 °C. Furthermore, Ti-in-biotite geothermometry provides an independent  
592 dataset indicating a prograde evolution with peak metamorphic temperatures reached between  
593 660 and 730 °C. Interestingly, our Ti-in-biotite estimates overlap with the 600 – 700 °C  
594 estimates obtained by Caggianelli et al. (2018) on samples distributed on the whole Calamita  
595 peninsula, although these authors discarded these estimates, based on the interpretation that  
596 retrograde muscovite was in equilibrium with the peak mineral assemblage. Though andalusite  
597 was not present in the sample investigated for phase equilibrium modeling, it occurs in the rocks  
598 nearby. The equilibrium textures of andalusite in the presence of melt (e.g. Fig. 3a), observed  
599 both in Punta Bianca and Capo Calvo, are indicative of very low-pressures of partial melting, in  
600 a fairly restricted P-T field between 0.1 and 0.25 GPa (Cesare et al., 2003). Therefore, the  
601 maximum pressure for partial melting can be set at 0.2 – 0.25 GPa. Pressures < 0.2 GPa has  
602 already been proposed for the metamorphism of these rocks (Duranti et al., 1992; Musumeci and  
603 Vaselli, 2012; Caggianelli et al., 2018), although anatexis was not considered. Moreover, the  
604 coexistence of melt and andalusite is an indication of fluid-present melting, because the dry  
605 granitic solidus do not intersect the andalusite stability field (see Le Breton and Thompson, 1988

606 and Cesare et al., 2003). Continuous melting in the presence of biotite without generating  
607 orthopyroxene as a peritectic phase indicates that partial melting occurred well below the biotite  
608 dehydration melting reaction (Le Breton and Thompson, 1988; Vielzeuf and Holloway, 1988),  
609 consuming the water available in the sample at and below the 'wet' granite solidus (e.g. Brown,  
610 2002; White and Powell, 2002; Guernina and Sawyer, 2003; Vernon and Clarke, 2008).  
611 Retention of water is expected during rapid heating of low-grade metapelites in contact aureoles,  
612 in contrast to regional metamorphism which renders metapelitic rocks more dehydrated (Buick et  
613 al., 2004).

614 Phase equilibrium modeling suggests melt productivity in the investigated sample (IESP3CS42A)  
615 between 1 and 4% in the cordierite + biotite + K-feldspar + plagioclase + ilmenite + melt field,  
616 assuming a water-saturated solidus (Fig. 13). An independent estimate, based on image analysis  
617 of the investigated sample, places the maximum amount of melt that was present at ~ 6% (area  
618 occupied by K-feldspar and plagioclase aggregates; Fig. 7a). This, however, represents an excess  
619 estimate, since feldspar aggregates preserve microstructural evidence of the presence of residual  
620 grains. Therefore, it is largely unlikely that they were completely molten.

621 Nevertheless, the maximum estimate of 6% melt is still below the 'melt connectivity transition'  
622 (7-8%) of Rosenberg and Handy (2005), suggesting that melt largely remained in situ. Indeed,  
623 structures indicating migration of melt such as dykelets or veins have not been observed in Capo  
624 Calvo.

625

## 626 **8.2 Deformation in the presence of melt: effect on structures and microstructures**

627 The Calamita Schists are characterized by a heterogeneous pattern of deformation which has  
628 been detailed by Papeschi et al. (2017, 2018). However, the processes that allowed shear-zone

629 initiation in the Calamita Unit remained unclear, in particular regarding the transition from a  
630 relatively distributed upper amphibolite-facies deformation with respect to narrow and localized  
631 greenschist-facies shear zones (Papeschi et al., 2017, 2018).

632 In the investigated Capo Calvo and Punta Bianca sections, the mesoscale foliation is more  
633 penetrative and the average grain size is finer in light-colored domains, in which significant  
634 amounts of K-feldspar, plagioclase and quartz are present (Fig. 2d, 2e, 3b). Quartz shows  
635 deformational features like lobate grain boundaries, amoeboid shape, pinning microstructures,  
636 and island grains (e.g. Fig. 7b, c) that suggest deformation by grain boundary migration  
637 recrystallization, typical of rocks deformed at conditions of high metamorphic grade (e.g. Stipp  
638 et al., 2002; documented in detail for the Calamita Schists by Papeschi et al., 2017). On the other  
639 hand, K-feldspar + plagioclase + quartz aggregates very rarely show recrystallized grains and/or  
640 undulose extinction. In fact, they are dominated by euhedral and polygonal grains with triple  
641 junctions and straight grain boundaries, relatively uniform grain size of 100 – 400  $\mu\text{m}$ , spatially  
642 associated with interstitial grains (Fig. 5d among others), suggesting crystallization from melt  
643 (see sect. 6). The undeformed appearance of K-feldspar + plagioclase + quartz aggregates, largely  
644 displaying an igneous texture that did not experience significant subsolidus recrystallization, is in  
645 striking contrast with (1) the wellfoliated structure of light-colored domains at the mesoscale  
646 (Fig. 2e), (2) the extensive dynamic recrystallization of the associated quartz (Fig. 5a), and (3)  
647 the strong elongation of feldspar aggregates (Fig. 5b). A key observation is that ephemeral  
648 structures, which are easily erased by dynamic recrystallization, such as (1) interstitial phases,  
649 (2) pseudomorphs after films of former melt with very-low apparent dihedral angle and (3) lobes  
650 of K-feldspar and quartz are wellpreserved and appear largely unaffected by dynamic  
651 recrystallization and/or annealing in high-strain zones. Furthermore, there are neither strain caps

652 nor strain shadows surrounding feldspar aggregates, suggesting that melt-related structures were  
653 preserved at the grain scale and not obliterated by subsequent subsolidus deformation (i.e. they  
654 represented low-strain domains during development of amphibolite- to greenschist-facies shear  
655 zones). Similar microstructures, reported from granulite-facies high-strain zones, have been  
656 interpreted by Stuart et al. (2018) as evidence of deformation in the presence of melt, which can  
657 be achieved by grain boundary sliding, accommodated by the movement of interstitial melt along  
658 grain boundaries and porosity (Rosenberg and Handy, 2000; Rosenberg, 2001; Walte et al.,  
659 2005). Intergranular films of melt are indeed very common in the investigated high-strain rocks  
660 (e.g. Fig. 8d) and likely assisted the relative sliding of solid grains past each other during  
661 deformation. Deformation dominated by melt-assisted grain boundary sliding, rather than  
662 dislocation creep, is supported by the general lack of crystallographic preferred orientation in K-  
663 feldspar + quartz + plagioclase aggregates (e.g. Zavada et al., 2007; Viegas et al., 2016).  
664 Furthermore, during melt-accommodated grain boundary sliding, the solid grains did not  
665 experience solid-state deformation or migration of grain boundaries (Stuart et al., 2018).  
666 According to Dell'Angelo et al. (1987), Dell'Angelo and Tullis (1988), and Walte et al. (2005),  
667 at low melt fractions (likely between 1 and 4%) melt-assisted grain boundary sliding becomes  
668 ineffective and deformation switches to dislocation creep. The general lack of a subsolidus  
669 overprint on igneous features in feldspar aggregates and, in particular, the preservation of  
670 pseudomorphs after melt-filled pores indicates that the deactivation of melt-assisted grain  
671 boundary sliding determined a halt or decrease of deformation intensity following melt  
672 crystallization.

673

### 674 **8.3 Strain localization during and after partial melting**

675 The coexistence of localized igneous features with dynamic recrystallization in high-strain  
676 domains suggests that partial melting and deformation occurred together at peak metamorphic  
677 conditions in the Calamita Schists. The development of the foliation, which is more pervasive in  
678 light-colored and originally melt-rich domains with respect to dark-colored and originally melt-  
679 poor domains, clearly indicates a correlation between melt availability and intensity of  
680 deformation.

681 As quoted above, the presence of melt is an efficient softening mechanism even at very low melt  
682 fraction (e.g. Holyoke and Tullis, 2006; Zavada et al., 2007). On the other hand, crystallization  
683 of melt causes the deactivation of grain boundary sliding, leading to strain hardening of the  
684 system (Stuart et al., 2018). Therefore, while the presence of melt allows strain to be pervasively  
685 distributed, the switch to subsolidus deformation necessarily causes deformation to become more  
686 localized. Strain localization in narrow high-strain zones at subsolidus conditions allows the  
687 extensive preservation of fragile melt pseudomorphs formed close to peak metamorphic  
688 conditions.

689 The Calamita Schists record the transition from relatively distributed upper amphibolite-facies  
690 deformation in the presence of melt, preserved both at Capo Calvo and Punta Bianca, to  
691 localized, mylonitic deformation, well documented at Capo Calvo. Although mylonitic shear  
692 zones largely preserve greenschist-facies deformation (Papeschi et al., 2018), evidence of the  
693 transition from melt-present to subsolidus deformation is locally preserved in deformed schists in  
694 the shear zone walls (Fig. 9). Structures indicating former presence of melt, like interstitial grains  
695 (Fig. 10a), occur in aggregates wrapped by the metamorphic foliation and surrounded by strain  
696 caps. Quartz layers and K-feldspar + quartz + plagioclase aggregates are strongly affected by  
697 sub-solidus deformation, marked by (1) undulose extinction (Fig. 9b), (2) extensive

698 recrystallization of quartz and feldspar to mylonitic ribbons (Fig. 10c), and (3) development of a  
699 bimodal grain-size distribution due to coexisting relic and recrystallized grains (Fig. 9c,  
700 10c). Dynamic recrystallization of subparallel quartz and feldspathic layers is indicative of  
701 medium- to high-metamorphic grade deformation (see e.g. Vernon and Flood, 1987; Tullis et al.,  
702 2000; Hippertt et al., 2001). K-feldspar and plagioclase in particular are affected by extensive  
703 retrograde and synkinematic overgrowth of phyllosilicates that reflect the activity of reaction  
704 softening mechanisms (Mitra, 1978; White et al., 1980; Hippertt and Hongn, 1998; Mariani et  
705 al., 2006), which are commonly documented in mylonitic quartz-feldspathic rocks (e.g. Stünitz  
706 and Tullis, 2001). The retrograde growth of hydrous phyllosilicates demonstrates that water was  
707 available during deformation. The presence of fluids during deformation in high-strain zones of  
708 the Calamita Schists is also supported by a recent Electron Back Scatter Diffraction-based study  
709 that provided evidence of dissolution-precipitation creep in quartz during the development of  
710 mylonites (Papeschi and Musumeci, 2019).

711 Hydrous fluids might have acted as an efficient weakening component for the development of  
712 retrograde shear zones. Indeed, dynamic recrystallization of quartz and feldspar is favored under  
713 ‘wet’ conditions (hydrolytic weakening; Luan and Paterson, 1992; Post and Tullis, 1998; see also  
714 Vernon and Clarke, 2008). Localization of strain in the subsolidus region might hence be favored  
715 by the addition of external water. Circulation of fluids originated from the underlying plutonic  
716 system is well documented for the Calamita Schists (Dini et al., 2008). Moreover, the fluid  
717 released after crystallization of the melt might have infiltrated the Calamita Schists in a  
718 heterogeneous fashion, favoring strain partitioning in the fluid-rich portions of the aureole.  
719 Considering the investigated sections, we suggest that Punta Bianca was characterized by limited  
720 ingress of fluids after melt crystallization, whereas Capo Calvo was affected by fluid ingress



721 assisting strain localization during retrograde shearing. The latter scenario is supported by the  
722 strong sericitization of the peak metamorphic assemblage at Capo Calvo.

723

## 724 **9. Conclusions**

725 This study provides the first evidence of late Miocene migmatite formation in a very shallow  
726 aureole in the Northern Apennines and shows an example of retrograde strain partitioning and  
727 localization in patch migmatites in an upper crustal setting. The key results of this work can be  
728 summarized as follows:

729 (1) Phase equilibria modeling and Ti-in-biotite thermometry constrain partial melting via  
730 continuous biotite melting between 0.1 – 0.25 GPa and 660 – 710 °C in the andalusite  
731 field.

732 (2) Deformation concentrated in light-colored domains that represent leucosomes.  
733 Metamorphic quartz only displays extensive evidence of recrystallization by grain  
734 boundary migration and K-feldspar + quartz + plagioclase pseudomorphs after melt,  
735 which filled porosities, lack significant evidence of subsolidus deformation. Therefore,  
736 we suggest that deformation was assisted by melt-enhanced grain boundary sliding and  
737 ceased after crystallization of the melt.

738 (3) Melt crystallization determines strain hardening of the rocks, forcing a change in  
739 deformation style from distributed to localized in high-strain mylonitic shear zones.  
740 Mylonites preserve the transition from amphibolite-facies deformation in the presence of  
741 melt to dynamic recrystallization with the development of mylonitic ribbons.  
742 Heterogeneous fluid ingress is envisaged as being responsible for localized strain  
743 softening in high-strain zones during retrograde conditions.

744

## 745 **Acknowledgements**

746 The authors wish to thank Thomas Theye and Federico Lucci for many fruitful discussions and  
747 guidance with the microprobe. Paolo Garofalo and Luca Pandolfi are warmly thanked for access  
748 to their personal microscopy facilities. Omar Gianola is also thanked for assistance with the  
749 microscopy equipment in Padova.

750

751 **Funding:** this work was supported by the University of Pisa (PRA\_2016, Resp. Sergio Rocchi),  
752 by the PEGASO PhD program (Tuscany Region, Italy) and by the Erasmus+ exchange program  
753 of the European Union.

754

## 755 **Data Availability**

756 The microprobe source files (settings, core files and exported images), XRF analysis and phase  
757 equilibria modeling files related to this manuscript are available at Papeschi, Samuele;  
758 Musumeci, Giovanni; Massonne, Hans-Joachim (2019), “Microprobe and pseudosection data -  
759 Sample IESP3CS42A - Calamita Schists - Elba (Italy)”, Mendeley Data, V2  
760 <http://dx.doi.org/10.17632/c6ghw55sg4.2>

761

## 762 **Figure Captions**

763 **Figure 1**–(a)Simplified structural-geological map of Island of Elba (modified after Papeschi et  
764 al., 2017). The rectangle marks the insert of Fig. 1b. (b) Geological sketch map of the eastern  
765 coast of the Calamita peninsula, showing the position of the study areas, also with respect to the  
766 Ripalte antiform. Mineral abbreviations: And: andalusite; Bi: biotite; Cd: cordierite; Di:

767 diopside; Ksp: K-feldspar; Phl: phlogopite; Pl: plagioclase; Tr: tremolite; Wm: white mica; Wo:  
768 wollastonite.

769

770 **Figure 2 – (a-b)** Mesoscale features of the Calamita Schists in the Wm + Bi + Cd + And zone.

771 (a) Foliated micaschists with deformed quartz layers. (b) Folded quartz layers surrounded by

772 biotite-rich schists. The yellow dashed line highlights the fold pattern.(c-d-e-f) The Calamita

773 Schists at Punta Bianca (location in Fig. 1b), showing subparallel quartz layers, light-

774 coloredquartz-feldspar-rich domains and dark-coloredAnd/Cd + Bi domains that follow (c) folds

775 and (d) the main mesoscopic foliation. (e) Detail of the relationships between dark-colored and

776 light-colored domains, highlighting the increase in foliation intensity in light-colored domains.

777 (f) Andalusite-rich unfoliated dark-colored domain containing irregular Ksp + Pl + Q pockets.

778 Mineral abbreviations: And: andalusite; Bi: biotite; Cd: cordierite; Ksp: K-feldspar; Pl:

779 plagioclase; Q: quartz; Tur: tourmaline; Wm: white mica.

780

781 **Figure 3 - (a)** Sketch geological map of Capo Calvo with sample and figure locations. Poles to

782 the foliation and shear zones and stretching lineations are shown in the insert stereographic

783 projection (equal angle, lower hemisphere). The ellipse marks the trace of the 95% confidence

784 cone of the mean lineation vector (yellow star). (b-c) Mesoscale features at Capo Calvo: (b)

785 Transition from dark-colored, weakly foliated domains to light-colored, well-foliated domains.

786 Note the presence of deformed quartz layers. (c) Detail of light-colored domains showing well-

787 developed amphibolite-facies foliation crosscut by E-verging shear zones. The red arrows

788 highlight patches of K-feldspar + plagioclase + quartz. And: andalusite. Bi: biotite. Cd:

789 cordierite. Ksp: K-feldspar. Pl: plagioclase. Q: quartz.

790

791 **Figure 4** – Microstructures in dark-colored domains at Punta Bianca observed **(a-b-c-d)** under  
792 crossed polarized light (CPL) and **(e-f-g-h)** with the retardation plate inserted (CPL+RP). **(a)**  
793 General texture characterized by intergrowing decussate biotite grains, euhedral andalusite, and  
794 aggregates of K-feldspar, plagioclase, and quartz. The yellow rectangle highlights the location of  
795 Fig. 4d. **(b)** Foliated microstructure displaying subparallel biotite + ilmenite-, K-feldspar +  
796 plagioclase-, and quartz-rich layers. **(c)** K-feldspar + plagioclase + quartz-rich domain  
797 surrounding resorbed biotite grains. **(d)** Polygonal K-feldspar and quartz aggregate (white arrow)  
798 associated with misoriented biotite grains. **(e)** K-feldspar polycrystalline aggregate in contact  
799 with deformed quartz and biotite. The white arrow indicates an interstitial K-feldspar grain. **(f)**  
800 Orange-colored interstitial quartz with cusped lobes (white arrows) surrounding rounded grains  
801 (yellow arrow) and euhedral grains (green arrow). Mineral abbreviations: And: andalusite; Bi:  
802 biotite; Cd: cordierite; Ilm: ilmenite; Ksp: K-feldspar; Pl: plagioclase; Q: quartz; Wm: white  
803 mica.

804

805 **Figure 5** – Microstructures in light-colored domains at Punta Bianca. **(a)** Recrystallized quartz  
806 associated with elongated pseudomorphs of sericite over K-feldspar and plagioclase (CPL). **(b)**  
807 Recrystallized quartz-feldspar microstructure. Note the strongly elongated K-feldspar grains  
808 (CPL+RP). **(c)** Elongated K-feldspar + plagioclase aggregate (limits are contoured by the red  
809 dashed line) which follows a biotite-rich layer within quartz with amoeboid shape. The insert  
810 shows the resorbed outline of biotite (CPL). **(d)** Local polygonal texture with euhedral K-  
811 feldspar and quartz grain boundaries (red arrow) surrounded by interstitial K-feldspar with

812 cusped lobes (white arrows) (CPL+RP). Bi: biotite; Ilm: ilmenite; Ksp: K-feldspar; Pl:  
813 plagioclase; Q: quartz; Ser: sericite.

814

815 **Figure 6** – Microstructures in dark-colored domains at Capo Calvo: **(a)** General microfabric  
816 showing biotite – andalusite – cordierite and K-feldspar and Note the strongly lobate shape of  
817 biotite in the insert (yellow box) of**(a)**. **(b)** Interstitial K-feldspar lobes against metamorphic  
818 quartz. The small K-feldspar grains (white arrows) are all in optical continuity (CPL + RP).**(c)**  
819 Interstitial K-feldspar surrounding strongly resorbed biotite grains (CPL). **(d)** Detail of the K-  
820 feldspar + plagioclase + quartz aggregates showing interstitial quartz or K-feldspar grains (white  
821 arrows) and crystal faces (red arrows) (CPL + RP). And: andalusite; Bi: biotite; Cd: cordierite;  
822 Ilm: ilmenite; Ksp: K-feldspar; Pl: plagioclase; Q: quartz; Ser: sericite.

823

824 **Figure 7** – Microstructures in sample IESPCS42A, which is the representative of light-colored  
825 domains at Capo Calvo. **(a)** Thinsection scan showing the relative area (in %) of the different  
826 mineral phases. See text for details. **(b)** Quartz grains with lobate boundaries, amoeboid shape  
827 and dissection microstructures (yellow arrow)(CPL). **(c)** Strongly lobate quartz grains showing  
828 pinning and window microstructures (white arrow). Biotite grains define the metamorphic  
829 foliation (CPL). **(d)** Pseudomorphosed cordierite porphyroblasts surrounded by foliated quartz  
830 and biotite grains. SEM back scattered electron image. **(e)** K-feldspar-rich aggregate surrounded  
831 by quartz and biotite and characterized by a poikiloblastic microstructure due to biotite  
832 inclusions (CPL). Note the small K-feldspar lobes protruding in quartz (yellow arrows). Bi:  
833 biotite. Cd: cordierite. Ksp: K-feldspar. Pl: plagioclase. Q: quartz.

834

835 **Figure 8** – Microstructures in sample IESPCS42A (continues).**(a)** BSE image of Fig. 7e showing  
836 the poikiloblastic microstructure of K-feldspar, related to resorbed (light blue arrow) and  
837 euhedral biotite inclusions (see insert). Note both the cusped K-feldspar lobes (red arrows) and  
838 the thin layer of K-feldspar following a biotite-rich layer in quartz (green arrow) (BSE). **(b)**  
839 Detail of the interstitial K-feldspar lobes (white arrows) occurring at the contact between  
840 feldspar aggregates and quartz (location in Fig. 8b). Feldspar is bluish whereas quartz is reddish  
841 (CPL + RP).**(c)** Interstitial K-feldspar showing lobate contacts with quartz and biotite. The red  
842 arrows mark feldspar lobes with very low apparent dihedral angle against quartz. Note the  
843 presence of crystal faces in quartz at the contact with K-feldspar (BSE). **(d)** Interstitial K-feldspar  
844 interposed between quartz and biotite and within biotite grains (BSE). **(e)** Crystal faces (white  
845 arrows) at the contact between euhedral to subhedral K-feldspar, quartz, and plagioclase grains  
846 (CPL + RP). **(f)** Feldspar grains showing rounded outline (light blue) surrounded by interstitial  
847 K-feldspar and plagioclase (orange – reddish) (CPL + RP). Bi: biotite; Ksp: K-feldspar; Pl:  
848 plagioclase; Q: quartz.

849  
850 **Figure 9** – Microstructures in schists associated to shear zones.**(a)** Photo stitching of a  
851 thin section of sample IESPSP196 (CPL). The different colors show the relative area % occupied  
852 by the phases present for shear zone (top) and wall rock (bottom) subdomains. **(b)** Quartz and  
853 biotite layers defining the foliation. Note the extensive recrystallization along quartz rims and  
854 undulose extinction in biotite (CPL). **(c)** Serrated quartz aggregates developed along grain  
855 boundaries of larger grains (CPL). **(d)** Sheared, poikiloblastic K-feldspar aggregates wrapped by  
856 biotite and quartz (CPL). **(e)** Detail of the strain caps surrounding feldspar aggregates (red

857 arrow), characterized by recrystallized quartz and fine-grained white mica and biotite (CPL).Bi:  
858 biotite. Chl: chlorite Ksp: K-feldspar. Pl: plagioclase. Q: quartz. Wm: white mica.

859  
860 **Figure 10** – Microstructures in schists associated to shear zones (continues) **(a)** Interstitial quartz  
861 surrounding subhedral K-feldspar grains locally showing resorbed grain boundaries (CPL). **(b)**  
862 Crystal faces (red arrow) associated with more lobate boundaries between K-feldspar and quartz.  
863 Note the small K-feldspar inclusion (orange colors) with serrated grain boundaries (CPL + RP).  
864 **(c)** Recrystallized fine-grained K-feldspar ribbons being parallel to quartz layers. Note the  
865 mixing between K-feldspar and white mica in the upper-right corner (CPL). **(d)** Sericite-rich  
866 layers containing minor biotite and retrogressed cordierite, stretched parallel to the foliation.  
867 Scattered K-feldspar relics are present (CPL). Bi: biotite. Chl: chlorite. Ksp: K-feldspar. Pl:  
868 plagioclase. Q: quartz. Ser: sericite. Wm: white mica.

869  
870  
871 **Figure 11** – Compositional maps of sample IESPCS42A. **(a-b)** BSE-Images showing the  
872 location of compositional maps on **(a)** resorbed biotite aligned on the foliation (X-Ray Map 1)  
873 and **(b)** resorbed and euhedral biotite included in poikiloblastic K-feldspar (X-Ray Map 2). **(c-d-**  
874 **e-f-g-h)** Compositional maps showing the distribution of **(c-f)** Fe, **(d-g)** Al, **(e-h)**and Ti in **(c-d-**  
875 **e)**X-Ray Map 1 and **(f-g-h)**X-Ray Map 2. See text for a detailed comment.Bi: biotite. Chl:  
876 chlorite. Ilm: ilmenite; Ksp: K-feldspar. Pl: plagioclase. Ser: sericite. Ru: rutile.

877  
878 **Figure 12** - **(a)**  $X_{Fe}$  – total  $Al^{IV}$  p.f.u. diagram showing the classification of the analyzed biotite,  
879 following Deer et al. (1992); **(b)** Compositional variability of biotite in the  $X_{Fe}$  –  $Ti$  p.f.u.

880 space.(c)Results of Ti-in-biotite geothermometrybased on the geothermometer by Wu and Chen  
881 (2015).

882  
883 **Figure 13** – P-T pseudosections of sample IESP3CS42A (microstructures in Fig. 7 and  
884 8)modeledin the MnNCKFMASHT system. The subsolidus part was calculated assuming excess  
885 H<sub>2</sub>O while the suprasolidus regionwas calculated with a fixed1.66 mol% H<sub>2</sub>O content (0.5 vol%  
886 of water at 0.2 GPa at the solidus). Quartz is present in all fields. X<sub>Fe</sub> isopleths for biotite (yellow  
887 dashed lines) and cordierite (blue dashed lines) are shown. Black dashed lines are the melt  
888 isomodes. The red line marks the solidus.And: andalusite Bi: biotite. Cd: cordierite. Chl: chlorite.  
889 G: garnet. Ilm: ilmenite. Liq: melt. Mu: muscovite. Opx: orthopyroxene. Pl: plagioclase. Q:  
890 quartz. Sill: sillimanite. Ru: rutile.

891

## 892 **Table captions**

893

894 **Table 1** – Radiometric ages in samples of metamorphic and igneous rocks from the Calamita  
895 peninsula, after a: Musumeci et al. (2011); b: Musumeci et al. (2015) and c: Viola et al. (2018).  
896 And = andalusite; Bi = biotite; Cd = cordierite; Di = diopside; Phl = phlogopite.

897

898 **Table 2** – Representative analyses of biotite, pinitized cordierite, K-feldspar, plagioclase,  
899 ilmenite, and white mica in sample IESP3CS42A. T is the temperature estimated using the Ti-in-  
900 biotite geothermometer by Wu and Chen (2015). Ksp = K-feldspar. Ilm = ilmenite. Wm = white  
901 mica.



902 **References**

903 Barberi, F., Innocenti, F., Ricci, C.A., 1967. Il complesso scistoso di Capo Calamita  
904 (Isolad'Elba). *Atti della Società Toscana di Scienze Naturali residente a Pisa, Memorie, Serie A*  
905 *72*, 579–617.

906

907 Barboni, M., Annen, C., Schoene, B., 2015. Evaluating the construction and evolution of upper  
908 crustal magma reservoirs with coupled U/Pb zircon geochronology and thermal modeling: A  
909 case study from the Mt. Capanne pluton (Elba, Italy). *Earth and Planetary Science Letters* *432*,  
910 436-448.

911

912 Brown, M., 2002. Retrograde processes in migmatites and granulites revisited. *Journal of*  
913 *Metamorphic Geology* *20*, 25-40.

914

915 Brown, M., 2010. Melting of the continental crust during orogenesis: the thermal, rheological,  
916 and compositional consequences of melt transport from lower to upper continental  
917 crust. *Canadian Journal of Earth Sciences* *47*, 655-694.

918

919 Buick, I. S., Stevens, G., Gibson, R. L., 2004. The role of water retention in the anatexis of  
920 metapelites in the Bushveld Complex Aureole, South Africa: an experimental study. *Journal of*  
921 *Petrology* *45*(9), 1777-1797.

922

923 Cesare, B., Marchesi, C., Hermann, J., Gómez-Pugnaire, M. T., 2003. Primary melt inclusions in  
924 andalusite from anatectic graphitic metapelites: implications for the position of the  $Al_2SiO_5$   
925 triple point. *Geology* 31(7), 573-576.

926

927 Coggon, R., Holland, T. J. B., 2002. Mixing properties of phengitic micas and revised garnet-  
928 phengite thermobarometers. *Journal of Metamorphic Geology* 20, 683-696.

929

930 Cooper, R. F., Kohlstedt, D. L., 1984. Solution-precipitation enhanced diffusional creep of  
931 partially molten olivine-basalt aggregates during hot-pressing. *Tectonophysics* 107, 207-233.

932

933 Davidson, C., Schmid, S. M., Hollister, L. S., 1994. Role of melt during deformation in the deep  
934 crust. *Terra Nova* 6, 133-142.

935

936 Deer, W., Howie, R., Zussman, J., 1992. *An Introduction to the Rock-forming Minerals*, second  
937 ed. Pearson Education Ltd., Harlow, England.

938

939 Dell'Angelo, L. N., Tullis, J., 1988. Experimental deformation of partially melted granitic  
940 aggregates. *Journal of Metamorphic Geology* 6, 495-515.

941

942 Dell'Angelo, L. N., Tullis, J., Yund, R. A., 1987. Transition from dislocation creep to melt-  
943 enhanced diffusion creep in fine-grained granitic aggregates. *Tectonophysics* 139, 325-332.

944

945 Diener, J. F., Fagereng, Å., 2014. The influence of melting and melt drainage on crustal rheology  
946 during orogenesis. *Journal of Geophysical Research: Solid Earth*119, 6193-6210.  
947

948 Diener, J. F. A., Powell, R., White, R. W., Holland, T. J. B., 2007. A new thermodynamic model  
949 for clino- and orthoamphiboles in the system Na<sub>2</sub>O–CaO–FeO–MgO–Al<sub>2</sub>O<sub>3</sub>–SiO<sub>2</sub>–H<sub>2</sub>O–  
950 O. *Journal of Metamorphic Geology* 25, 631-656.  
951

952 Diener, J. F., Fagereng, Å., Thomas, S. A., 2016. Mid-crustal shear zone development under  
953 retrograde conditions: pressure–temperature–fluid constraints from the Kuckaus Mylonite Zone,  
954 Namibia. *Solid Earth*7, 1331-1347.  
955

956 Dini, A., Innocenti, F., Rocchi, S., Tonarini, S., Westerman, D. S., 2002. The magmatic  
957 evolution of the late Miocene laccolith–pluton–dyke granitic complex of Elba Island,  
958 Italy. *Geological Magazine*139, 257-279.  
959

960 Droop, G. T. R., Brodie, K. H., 2012. Anatectic melt volumes in the thermal aureole of the Etive  
961 Complex, Scotland: the roles of fluid-present and fluid-absent melting. *Journal of Metamorphic  
962 Geology*30, 843-864.  
963

964 Duranti, S., Palmeri, R., Pertusati, P. C., Ricci, C. A., 1992. Geological evolution and  
965 metamorphic petrology of the basal sequences of eastern Elba (complex II). *Acta  
966 Vulcanologica* 2, 213-229.  
967

968 Gapais, D., 1989. Shear structures within deformed granites: mechanical and thermal  
969 indicators. *Geology* 17(12), 1144-1147.

970

971 Guernina, S., Sawyer, E. W., 2003. Large-scale melt-depletion in granulite terranes: an example  
972 from the Archean AshuanipiSubprovince of Quebec. *Journal of Metamorphic Geology* 21, 181-  
973 201.

974

975 Henry, D. J., Guidotti, C. V., Thomson, J. A., 2005. The Ti-saturation surface for low-to-medium  
976 pressure metapeliticbiotites: Implications for geothermometry and Ti-substitution  
977 mechanisms. *American Mineralogist* 90(2-3), 316-328.

978

979 Hippertt, J. F., Hongn, F. D., 1998. Deformation mechanisms in the mylonite/ultramylonite  
980 transition. *Journal of Structural Geology* 20, 1435-1448.

981

982 Hippertt, J., Rocha, A., Lana, C., Egydio-Silva, M., Takeshita, T., 2001. Quartz plastic  
983 segregation and ribbon development in high-grade striped gneisses. *Journal of Structural*  
984 *Geology* 23(1), 67-80.

985

986 Holland, T. J. B., Powell, R., 1998. An internally consistent thermodynamic data set for phases  
987 of petrological interest. *Journal of Metamorphic Geology* 16, 309-343.

988

989 Holland, T., Powell, R., 2003. Activity–composition relations for phases in petrological  
990 calculations: an asymmetric multicomponent formulation. *Contributions to Mineralogy and*  
991 *Petrology* 145, 492-501.

992

993 Hollister, L. S., Crawford, M. L., 1986. Melt-enhanced deformation: A major tectonic  
994 process. *Geology* 14, 558-561.

995

996 Holness, M. B., Clemens, J. D., 1999. Partial melting of the Appin quartzite driven by fracture-  
997 controlled H<sub>2</sub>O infiltration in the aureole of the Ballachulish Igneous Complex, Scottish  
998 Highlands. *Contributions to Mineralogy and Petrology* 136, 154-168.

999

1000 Holness, M. B., Sawyer, E. W., 2008. On the pseudomorphing of melt-filled pores during the  
1001 crystallization of migmatites. *Journal of Petrology* 49, 1343-1363.

1002

1003 Holness, M. B., Cesare, B., Sawyer, E. W., 2011. Melted rocks under the microscope:  
1004 microstructures and their interpretation. *Elements* 7(4), 247-252.

1005

1006 Holyoke III, C. W., Tullis, J. 2006. The interaction between reaction and deformation: an  
1007 experimental study using a biotite+ plagioclase+ quartz gneiss. *Journal of Metamorphic*  
1008 *Geology* 24(8), 743-762.

1009

1010 Jessell, M. W., 1987. Grain-boundary migration microstructures in a naturally deformed  
1011 quartzite. *Journal of Structural Geology* 9, 1007-1014.

1012

1013 Johnson, T. E., Gibson, R. L., Brown, M., Buick, I. S., Cartwright, I. A. N., 2003. Partial melting  
1014 of metapelitic rocks beneath the Bushveld Complex, South Africa. *Journal of Petrology* 44, 789-  
1015 813.

1016

1017 Karlstrom, K. E., Miller, C. F., Kingsbury, J. A., Wooden, J. L., 1993. Pluton emplacement along  
1018 an active ductile thrust zone, Piute Mountains, southeastern California: Interaction between  
1019 deformational and solidification processes. *Geological Society of America Bulletin* 105, 213-230.

1020

1021 Keller, J. V. A., Coward, M. P., 1996. The structure and evolution of the Northern Tyrrhenian  
1022 Sea. *Geological Magazine* 133, 1-16.

1023

1024 Kruckenberg, S.C., Vanderhaeghe, O., Ferré, E.C., Teyssier, C., Whitney, D.L., 2011. Flow of  
1025 partially molten crust and the internal dynamics of a migmatite dome, Naxos,  
1026 Greece. *Tectonics* 30.

1027

1028 Le Breton, N., Thompson, A. B., 1988. Fluid-absent (dehydration) melting of biotite in  
1029 metapelites in the early stages of crustal anatexis. *Contributions to Mineralogy and Petrology* 99,  
1030 226-237.

1031

1032 Luan, F. C., Paterson, M. S., 1992. Preparation and deformation of synthetic aggregates of  
1033 quartz. *Journal of Geophysical Research: Solid Earth* 97(B1), 301-320.

1034

1035 Mahar, E. M., Baker, J. M., Powell, R., Holland, T. J. B., Howell, N., 1997. The effect of Mn on  
1036 mineral stability in metapelites. *Journal of Metamorphic Geology* 15, 223-238.  
1037

1038 Marchildon, N., Brown, M., 2002. Grain-scale melt distribution in two contact aureole rocks:  
1039 Implications for controls on melt localization and deformation. *Journal of Metamorphic*  
1040 *Geology* 20, 381-396.  
1041

1042 Mariani, E., Brodie, K. H., Rutter, E. H., 2006. Experimental deformation of muscovite shear  
1043 zones at high temperatures under hydrothermal conditions and the strength of phyllosilicate-  
1044 bearing faults in nature. *Journal of Structural Geology* 28, 1569-1587.  
1045

1046 Massa, G., Musumeci, G., Mazzarini, F., Pieruccioni, D., 2017. Coexistence of contractional and  
1047 extensional tectonics during the northern Apennines orogeny: the late Miocene out-of-sequence  
1048 thrust in the Elba Island nappe stack. *Geological Journal* 52, 353-368.  
1049

1050 Mazzarini, F., Musumeci, G., Cruden, A. R., 2011. Vein development during folding in the  
1051 upper brittle crust: The case of tourmaline-rich veins of eastern Elba Island, northern Tyrrhenian  
1052 Sea, Italy. *Journal of Structural Geology* 33, 1509-1522.  
1053

1054 Miranda, E. A., Klepeis, K. A., 2016. The interplay and effects of deformation and crystallized  
1055 melt on the rheology of the lower continental crust, Fiordland, New Zealand. *Journal of*  
1056 *Structural Geology* 93, 91-105.  
1057

1058 Misra, S., Burg, J. P., Vigneresse, J. L., Mainprice, D., 2014. Rheological transition during large  
1059 strain deformation of melting and crystallizing metapelites. *Journal of Geophysical Research:*  
1060 *Solid Earth*119, 3971-3985.

1061

1062 Mitra, G., 1978. Ductile deformation zones and mylonites; the mechanical processes involved in  
1063 the deformation of crystalline basement rocks. *American Journal of Science* 278, 1057-1084.

1064

1065 Musumeci, G., Vaselli, L., 2012. Neogene deformation and granite emplacement in the  
1066 metamorphic units of northern Apennines (Italy): Insights from mylonitic marbles in the Porto  
1067 Azzurro pluton contact aureole (Elba Island). *Geosphere*8, 470-490.

1068

1069 Musumeci, G., Mazzarini, F., Tiepolo, M., Di Vincenzo, G., 2011. U-Pb and <sup>40</sup>Ar-<sup>39</sup>Ar  
1070 geochronology of Palaeozoic units in the northern Apennines: determining protolith age and  
1071 alpine evolution using the Calamita Schist and Ortano Porphyroid. *Geological Journal* 46, 288-  
1072 310.

1073

1074 Musumeci, G., Mazzarini, F., Cruden, A. R., 2015. The Zuccale Fault, Elba Island, Italy: a new  
1075 perspective from fault architecture. *Tectonics* 34, 1195-1218.

1076

1077 Papeschi, S., Musumeci, G., 2019. Fluid assisted strain localization in quartz at the brittle/ductile  
1078 transition. *Geochemistry, Geophysics, Geosystems*20, 3044-3064.

1079



1080 Papeschi, S., Musumeci, G., Mazzarini, F., 2017. Heterogeneous brittle-ductile deformation at  
1081 shallow crustal levels under high thermal conditions: The case of a synkinematic contact aureole  
1082 in the inner northern Apennines, southeastern Elba Island, Italy. *Tectonophysics*717, 547-564.  
1083

1084 Papeschi, S., Musumeci, G., Mazzarini, F., 2018. Evolution of shear zones through the brittle-  
1085 ductile transition: The Calamita Schists (Elba Island, Italy). *Journal of Structural Geology*113,  
1086 100-114.  
1087

1088 Passchier, C. W., Trouw, R. A. 2005. *Microtectonics*. Springer Science & Business Media.  
1089

1090 Pattison, D. R. M., Harte, B., 1988. Evolution of structurally contrasting anatectic migmatites in  
1091 the 3 kbar Ballachulish aureole, Scotland. *Journal of Metamorphic Geology* 6, 475-494.  
1092

1093 Pawley, M. J., Collins, W. J., 2002. The development of contrasting structures during the cooling  
1094 and crystallisation of a syn-kinematic pluton. *Journal of Structural Geology*24(3), 469-483.  
1095

1096 Platten, I.M., 1982. Partial melting of feldspathic quartzite around late Caledonian minor  
1097 intrusion in Appin, Scotland. *Geological Magazine* 119, 413-419.  
1098

1099 Post, A., Tullis, J., 1998. The rate of water penetration in experimentally deformed quartzite:  
1100 implications for hydrolytic weakening. *Tectonophysics*295, 117-137.  
1101

1102 Powell, R., Holland, T. J. B., 1988. An internally consistent dataset with uncertainties and  
1103 correlations: 3. Applications to geobarometry, worked examples and a computer  
1104 program. *Journal of Metamorphic Geology* 6, 173-204.

1105

1106 Rosenberg, C. L., 2001. Deformation of partially molten granite: a review and comparison of  
1107 experimental and natural case studies. *International Journal of Earth Sciences* 90(1), 60-76.

1108

1109 Rosenberg, C. L., Handy, M. R., 2000. Syntectonic melt pathways during simple shearing of a  
1110 partially molten rock analogue (Norcamphor-Benzamide). *Journal of Geophysical Research:*  
1111 *Solid Earth* 105(B2), 3135-3149.

1112

1113 Rosenberg, C. L., Handy, M. R., 2005. Experimental deformation of partially melted granite  
1114 revisited: implications for the continental crust. *Journal of Metamorphic Geology* 23, 19-28.

1115

1116 Rutter, E. H., Neumann, D. H. K., 1995. Experimental deformation of partially molten Westerly  
1117 granite under fluid-absent conditions, with implications for the extraction of granitic  
1118 magmas. *Journal of Geophysical Research: Solid Earth* 100, 15697-15715.

1119

1120 Sawyer, E. W., 1999. Criteria for the recognition of partial melting. *Physics and Chemistry of the*  
1121 *Earth, Part A: Solid Earth and Geodesy* 24, 269-279.

1122

1123 Sawyer, E. W., 2001. Melt segregation in the continental crust: distribution and movement of  
1124 melt in anatectic rocks. *Journal of Metamorphic Geology* 19(3), 291-309.

1125

1126 Sawyer, E. W., 2008. Atlas of migmatites. The Canadian Mineralogist, Special Publication 9.

1127 NRC Research Press, Ottawa, Ontario, Canada.

1128

1129 Schneider, C. A., Rasband, W. S., Eliceiri, K. W., 2012. NIH Image to ImageJ: 25 years of

1130 image analysis. *Nature Methods* 9, 671.

1131

1132 Schulmann, K., Martelat, J. E., Ulrich, S., Lexa, O., Štípská, P., Becker, J. K., 2008. Evolution of

1133 microstructure and melt topology in partially molten granitic mylonite: Implications for rheology

1134 of felsic middle crust. *Journal of Geophysical Research: Solid Earth* 113(B10).

1135

1136 Stipp, M., Stünitz, H., Heilbronner, R., Schmid, S. M., 2002. The eastern Tonale fault zone: a

1137 'natural laboratory' for crystal plastic deformation of quartz over a temperature range from 250

1138 to 700 °C. *Journal of Structural Geology* 24, 1861-1884.

1139

1140 Stuart, C. A., Piazzolo, S., Daczko, N. R., 2018. The recognition of former melt flux through

1141 high-strain zones. *Journal of Metamorphic Geology* 36, 1049-1069.

1142

1143 Stünitz, H., Tullis, J., 2001. Weakening and strain localization produced by syn-deformational

1144 reaction of plagioclase. *International Journal of Earth Sciences* 90, 136-148.

1145

1146 Tullis, J., Stünitz, H., Teyssier, C., Heilbronner, R., 2000. Deformation microstructures in  
1147 quartzo-feldspathic rocks. In: Jessel, M. W., Urai, J. L. (Eds.) Stress, strain and structure, a  
1148 volume in honour of W.D Means. *Journal of the Virtual Explorer*, 2.  
1149  
1150 Urai, J. L., Means, W. D., Lister, G. S., 1986. Dynamic recrystallization of minerals. *Mineral  
1151 and Rock Deformation: Laboratory Studies*, AGU Geophysical Monograph Series 36, 161-199.  
1152  
1153 Vanderhaeghe, O., 2009. Migmatites, granites and orogeny: Flow modes of partially-molten  
1154 rocks and magmas associated with melt/solid segregation in orogenic belts. *Tectonophysics* 477,  
1155 119-134.  
1156  
1157 Vernon, R. H., Clarke, G. L., 2008. *Principles of Metamorphic Petrology*. Cambridge University  
1158 Press, Cambridge, England.  
1159  
1160 Vernon, R. H., Flood, R. H., 1987. Contrasting deformation and metamorphism of S and I type  
1161 granitoids in the Lachian Fold Belt, Eastern Australia. *Tectonophysics* 147, 127-143.  
1162  
1163 Viegas, G., Menegon, L., Archanjo, C., 2016. Brittle grain-size reduction of feldspar, phase  
1164 mixing and strain localization in granitoids at mid-crustal conditions (Pernambuco shear zone,  
1165 NE Brazil). *Solid Earth* 7(2), 375-396.  
1166  
1167 Vielzeuf, D., Holloway, J. R., 1988. Experimental determination of the fluid-absent melting  
1168 relations in the pelitic system. *Contributions to Mineralogy and Petrology* 98, 257-276.

1169

1170 Vigneresse, J. L., Tikoff, B., 1999. Strain partitioning during partial melting and crystallizing  
1171 felsic magmas. *Tectonophysics* 312, 117-132.

1172

1173 Vigneresse, J. L., Barbey, P., Cuney, M., 1996. Rheological transitions during partial melting  
1174 and crystallization with application to felsic magma segregation and transfer. *Journal of*  
1175 *Petrology* 37, 1579-1600.

1176

1177 Viola, G., Torgersen, E., Mazzarini, F., Musumeci, G., van derLelij, R., Schönerberger, J.,  
1178 Garofalo, P. S., 2018. New Constraints on the Evolution of the Inner Northern Apennines by K-  
1179 Ar Dating of Late Miocene-Early Pliocene Compression on the Island of Elba,  
1180 Italy. *Tectonics* 37, 3229-3243.

1181

1182 Walte, N. P., Bons, P. D., Passchier, C. W., 2005. Deformation of melt-bearing systems—insight  
1183 from in situ grain-scale analogue experiments. *Journal of Structural Geology* 27(9), 1666-1679.

1184

1185 White, S. H., Burrows, S. E., Carreras, J., Shaw, N. D., Humphreys, F. J., 1980. On mylonites in  
1186 ductile shear zones. *Journal of Structural Geology* 2, 175-187.

1187

1188 White, R. W., Powell, R., 2002. Melt loss and the preservation of granulite facies mineral  
1189 assemblages. *Journal of Metamorphic Geology* 20, 621-632.

1190

1191 White, R. W., Powell, R., Holland, T. J. B., Worley, B. A., 2000. The effect of TiO<sub>2</sub> and Fe<sub>2</sub>O<sub>3</sub>  
1192 on metapelitic assemblages at greenschist and amphibolite facies conditions: mineral equilibria  
1193 calculations in the system K<sub>2</sub>O-FeO-MgO-Al<sub>2</sub>O<sub>3</sub>-SiO<sub>2</sub>-H<sub>2</sub>O-TiO<sub>2</sub>-Fe<sub>2</sub>O<sub>3</sub>. *Journal of*  
1194 *Metamorphic Geology* 18, 497-511.

1195

1196 White, R. W., Powell, R., Clarke, G. L., 2002. The interpretation of reaction textures in Fe-rich  
1197 metapelitic granulites of the Musgrave Block, central Australia: constraints from mineral  
1198 equilibria calculations in the system K<sub>2</sub>O-FeO-MgO-Al<sub>2</sub>O<sub>3</sub>-SiO<sub>2</sub>-H<sub>2</sub>O-TiO<sub>2</sub>-Fe<sub>2</sub>O<sub>3</sub>. *Journal of*  
1199 *Metamorphic Geology* 20, 41-55.

1200

1201 White, R. W., Pomroy, N. E., Powell, R., 2005. An in situ metatexite–diatexite transition in  
1202 upper amphibolite facies rocks from Broken Hill, Australia. *Journal of Metamorphic*  
1203 *Geology* 23, 579-602.

1204

1205 White, R. W., Powell, R., Holland, T. J. B., 2007. Progress relating to calculation of partial  
1206 melting equilibria for metapelites. *Journal of Metamorphic Geology* 25, 511-527.

1207

1208 Wu, C. M., Chen, H. X., 2015. Revised Ti-in-biotite geothermometer for ilmenite-or rutile-  
1209 bearing crustal metapelites. *Science Bulletin* 60(1), 116-121.

1210

1211 Yakymchuk, C., Brown, M., 2014. Consequences of open-system melting in tectonics. *Journal*  
1212 *of the Geological Society* 171, 21-40.

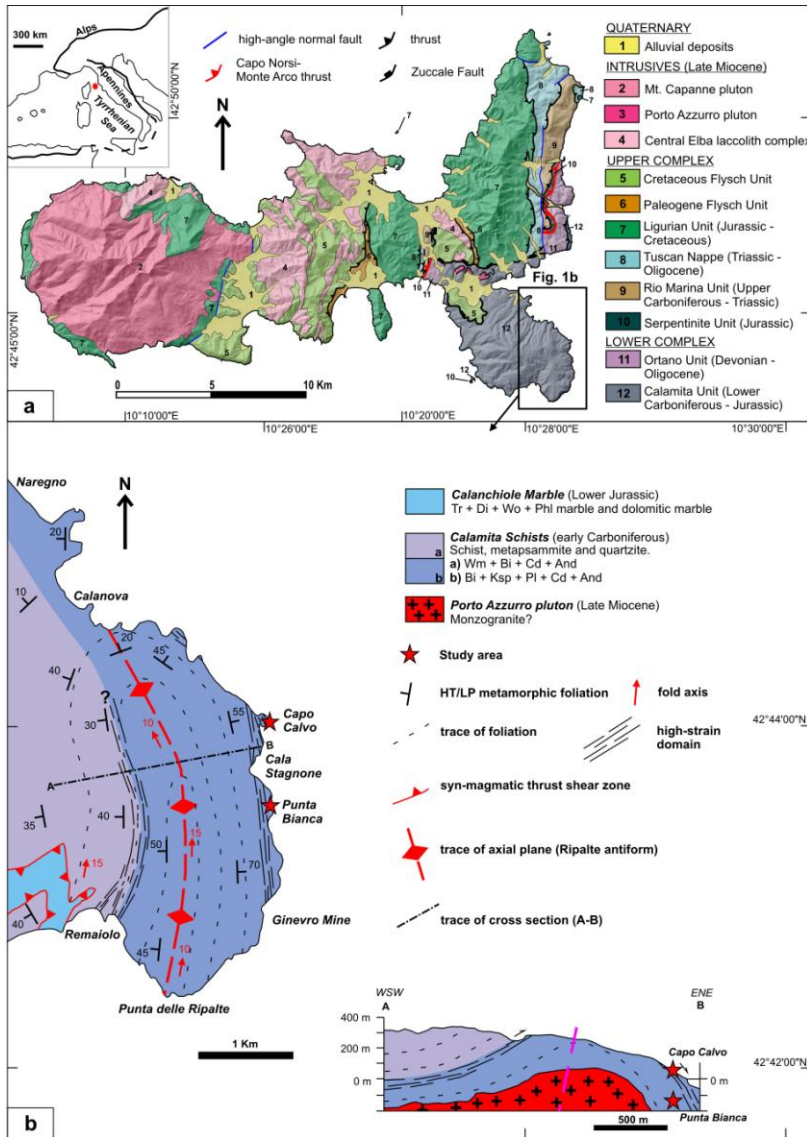
1213

1214 Závada, P., Schulmann, K., Konopásek, J., Ulrich, S., Lexa, O., 2007. Extreme ductility of  
1215 feldspar aggregates—Melt-enhanced grain boundary sliding and creep failure: Rheological  
1216 implications for felsic lower crust. *Journal of Geophysical Research: Solid Earth* 112.

1217

1218 Zibra, I., White, J. C., Menegon, L., Dering, G., Gessner, K., 2018. The ultimate fate of a  
1219 synmagmatic shear zone. Interplay between rupturing and ductile flow in a cooling granite  
1220 pluton. *Journal of Structural Geology* 110, 1-23.

1221



1222

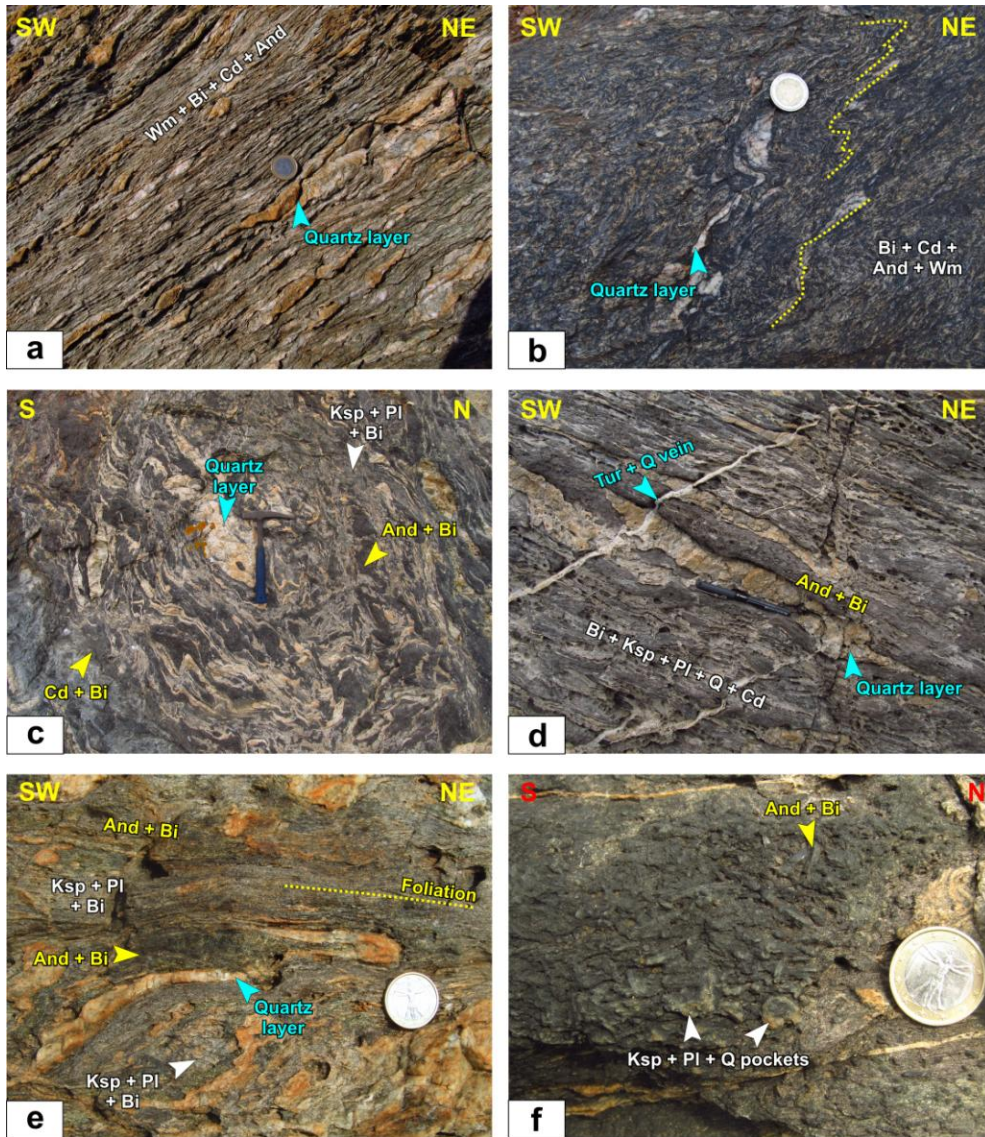
1223 Figure 1

1224

1225

1226





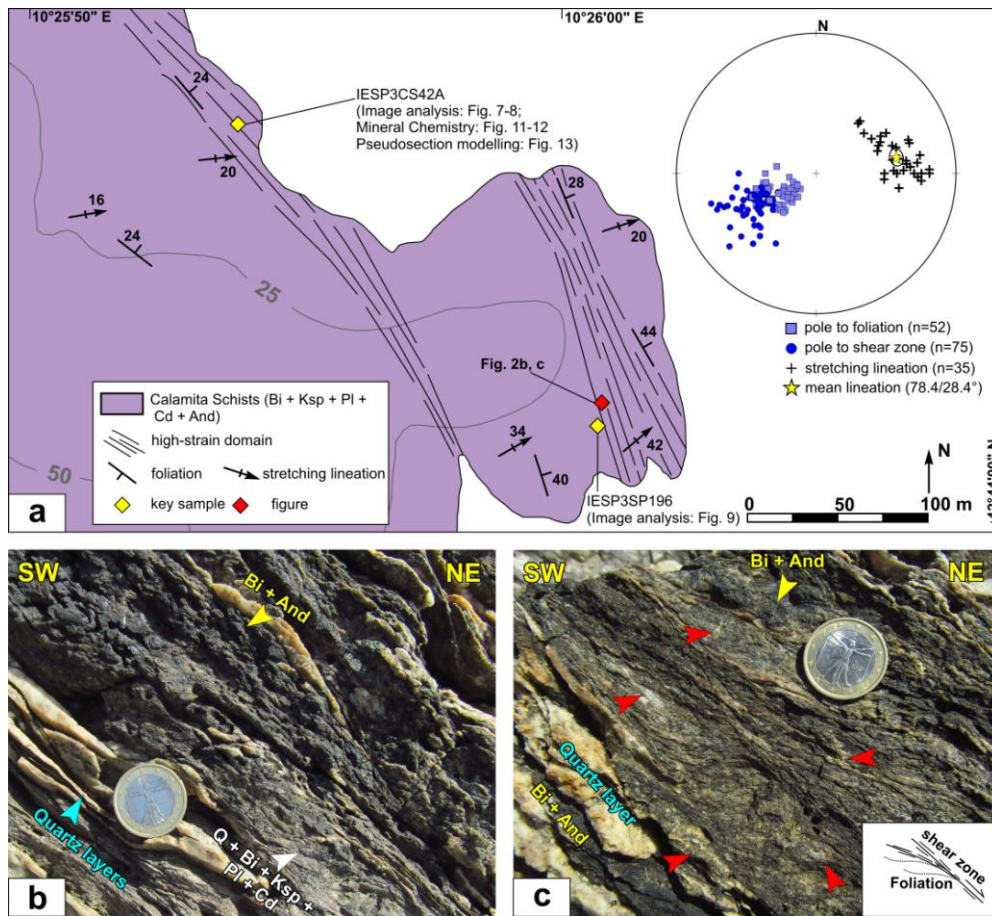
1227

1228 Figure 2

1229

1230

1231

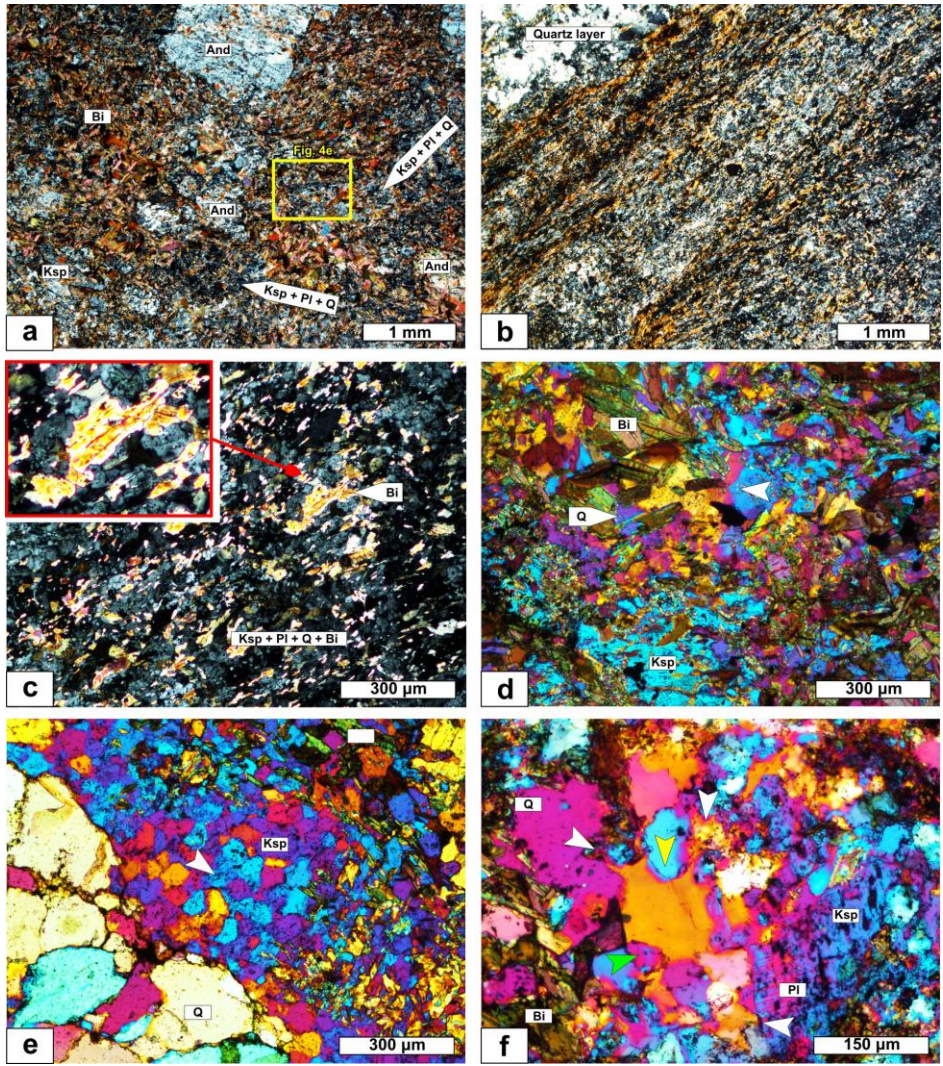


1232

1233 Figure 3

1234





1235

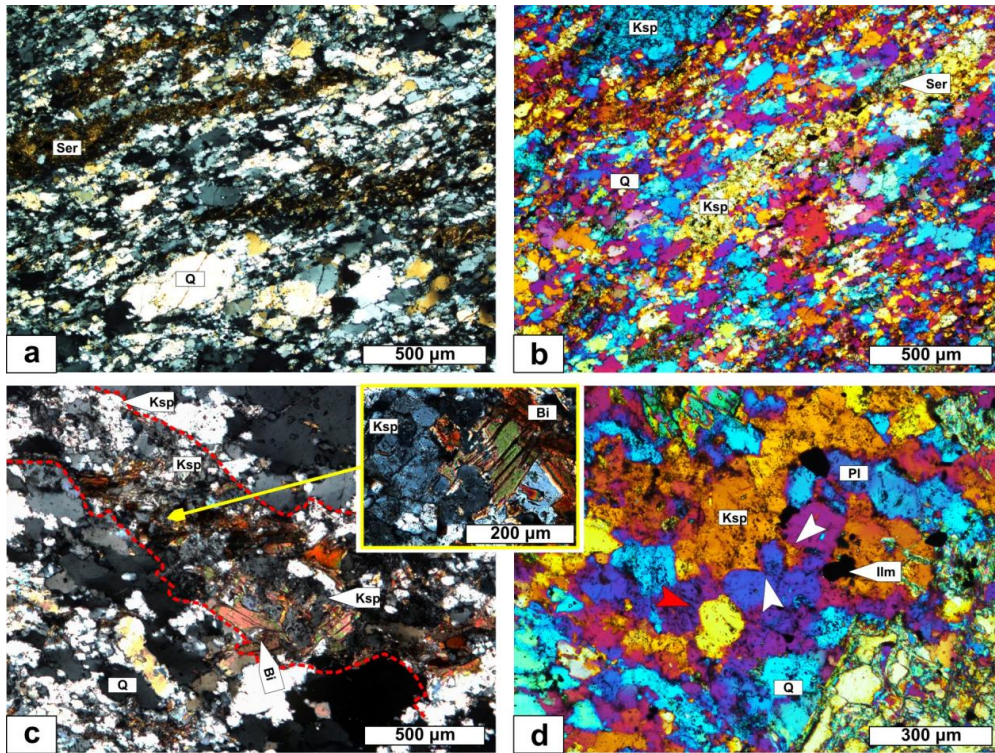
1236 Figure 4

1237

1238

1239

1240



1241

1242 Figure 5

1243

1244

1245

1246

1247

1248

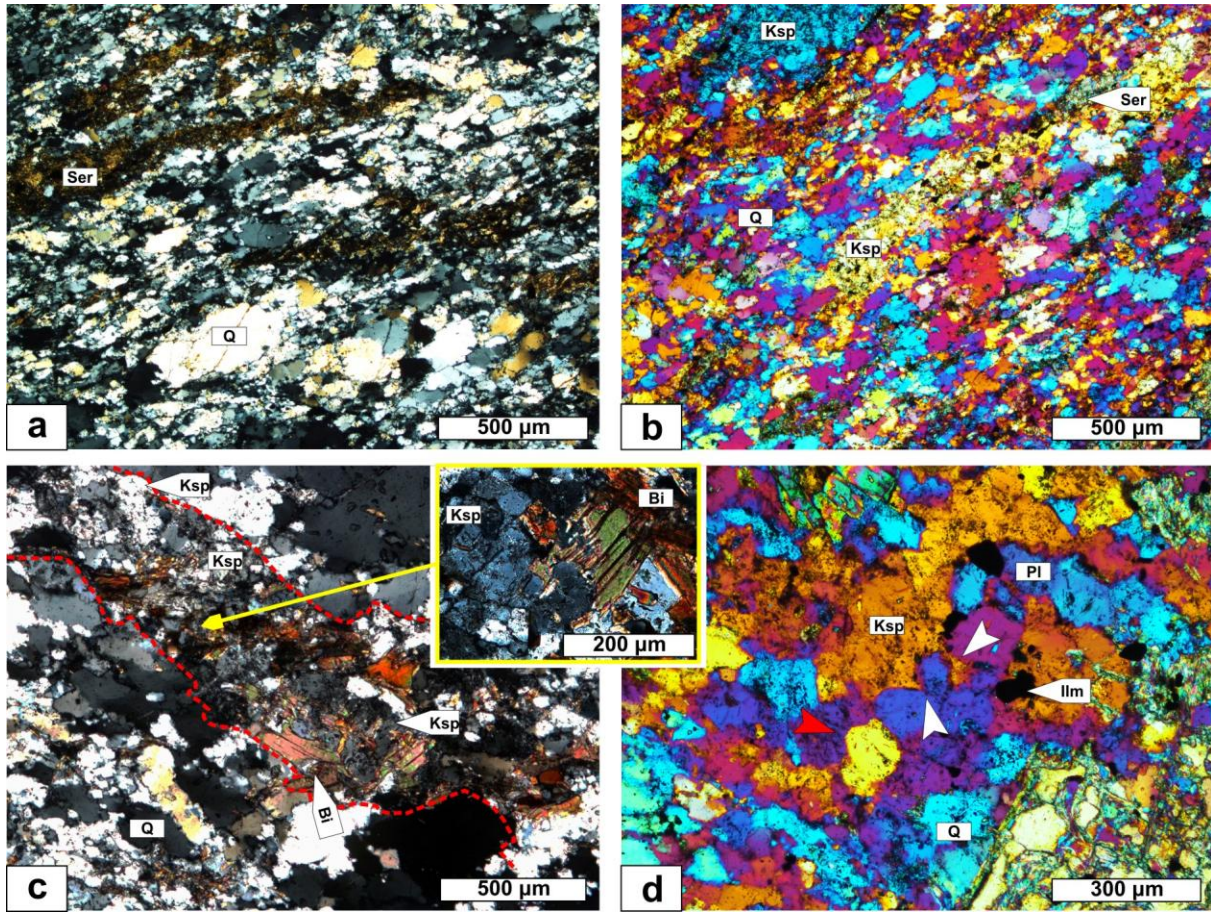
1249

1250

1251

1252





1253

1254 Figure 6

1255

1256

1257

1258

1259

1260

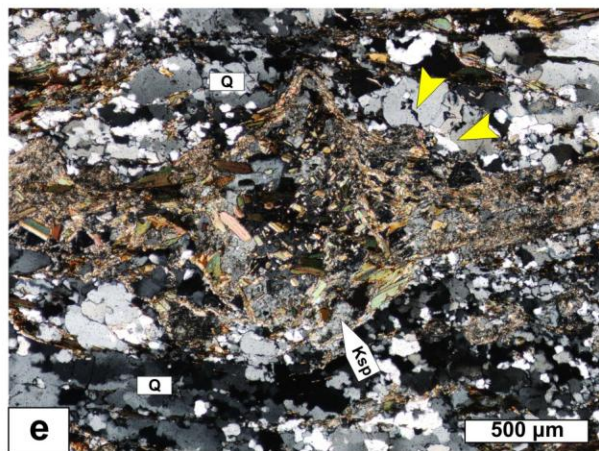
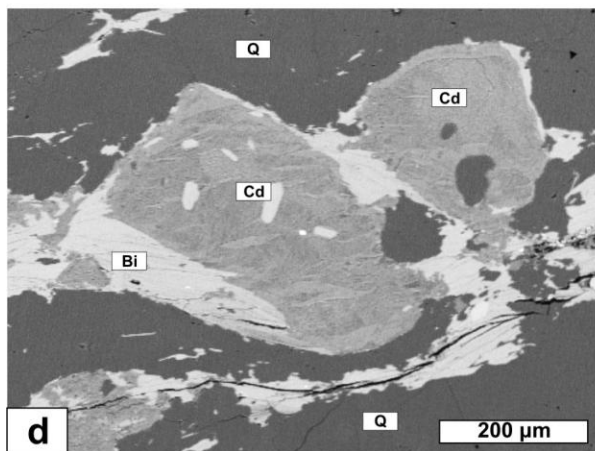
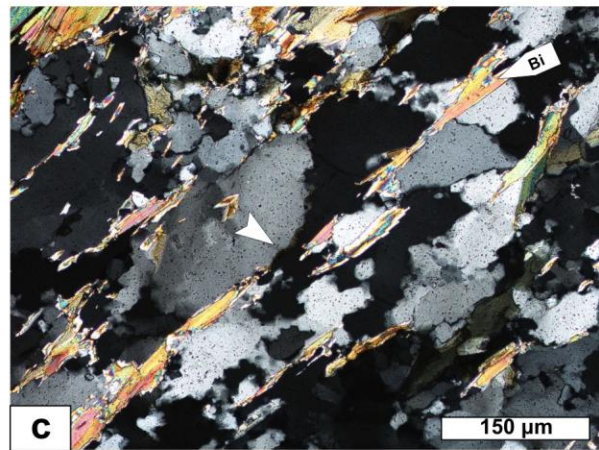
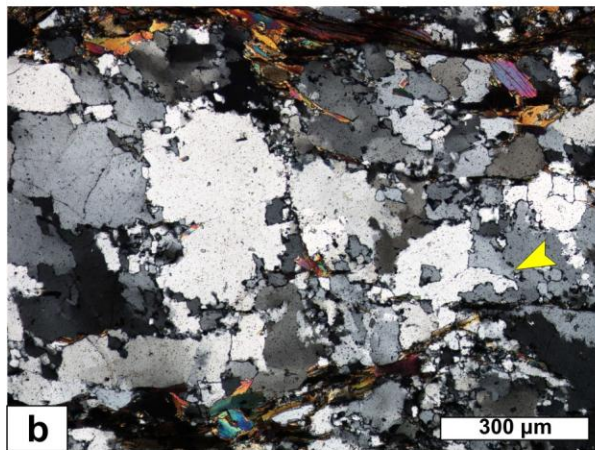
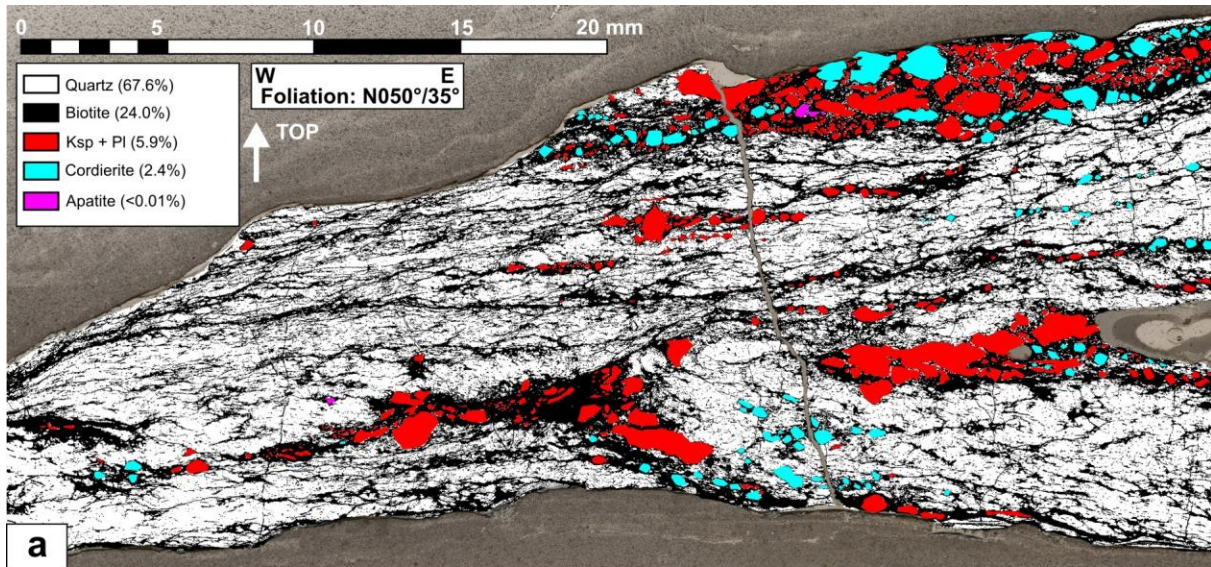
1261

1262

1263

1264





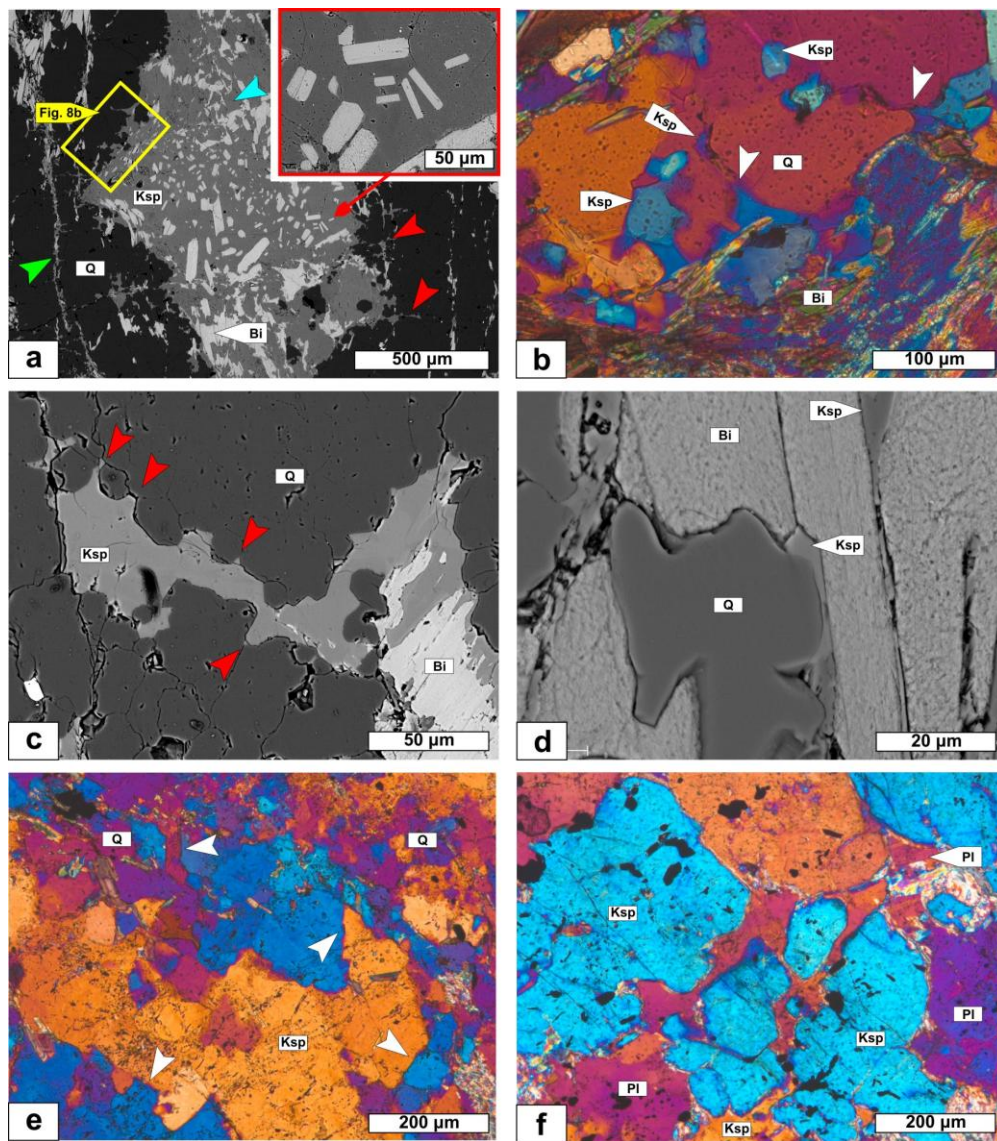
1265

1266 Figure 7

1267

1268



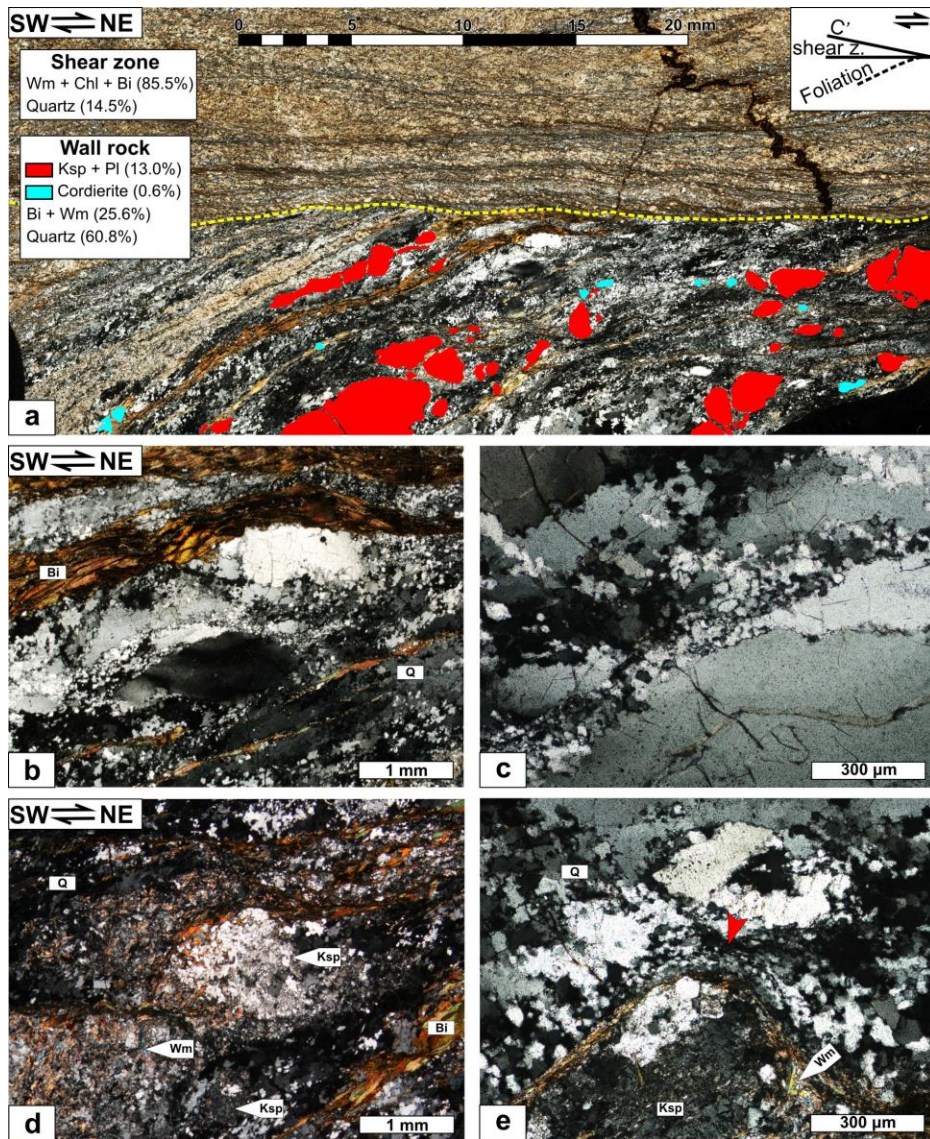


1270

1271 Figure 8

1272

1273



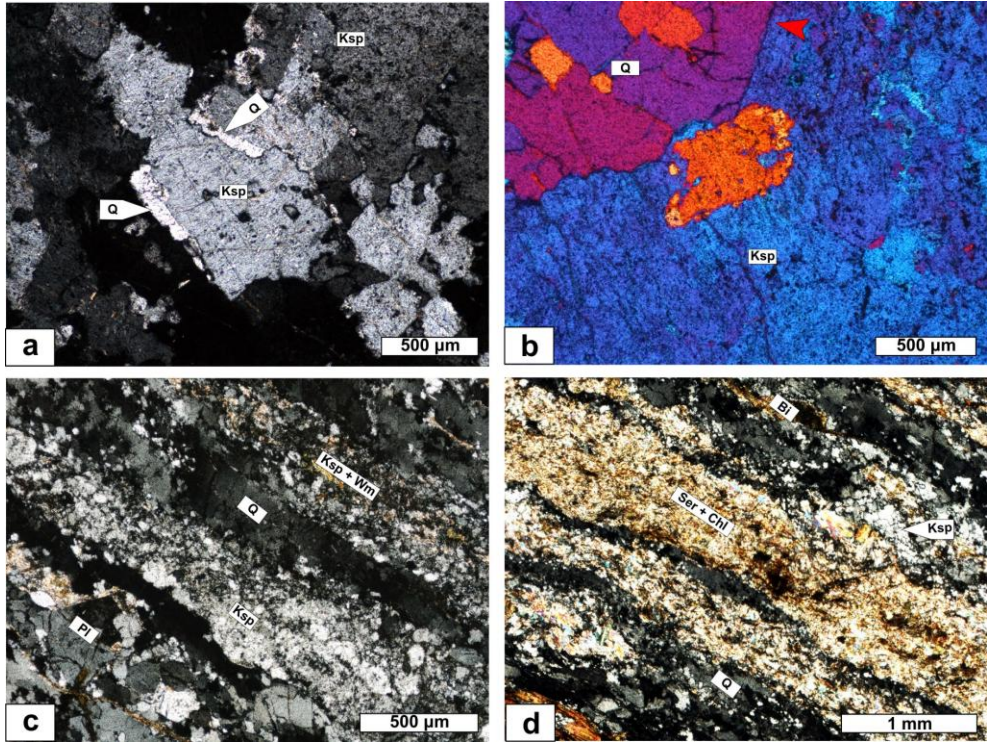
1274

1275 Figure 9

1276

1277



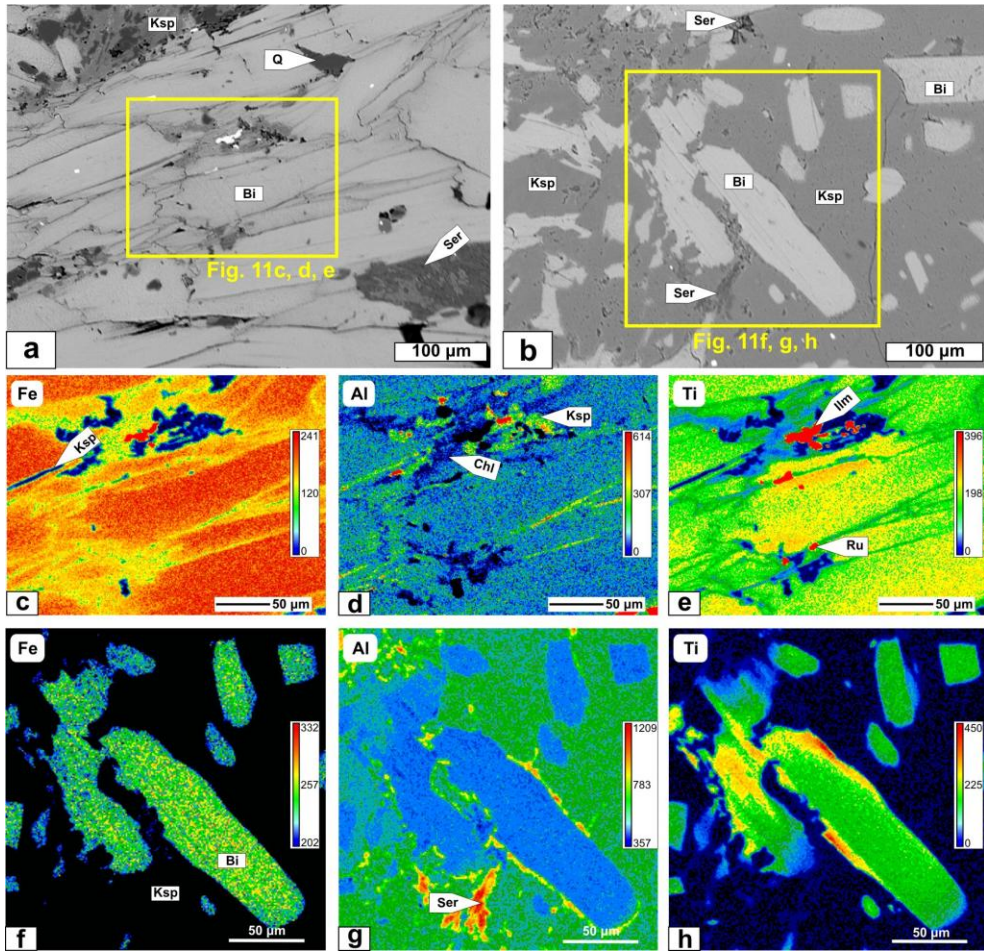


1278

1279 Figure 10

1280

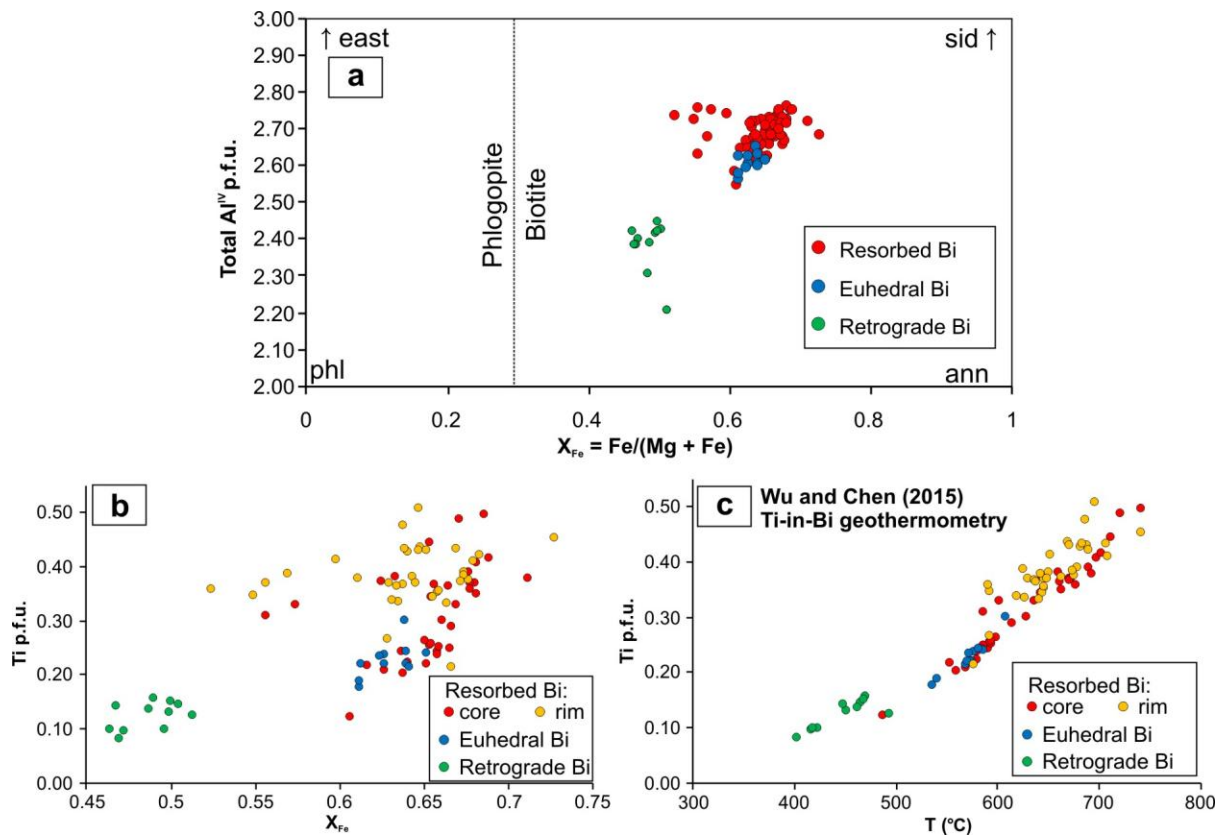
1281



1282

1283 Figure 11

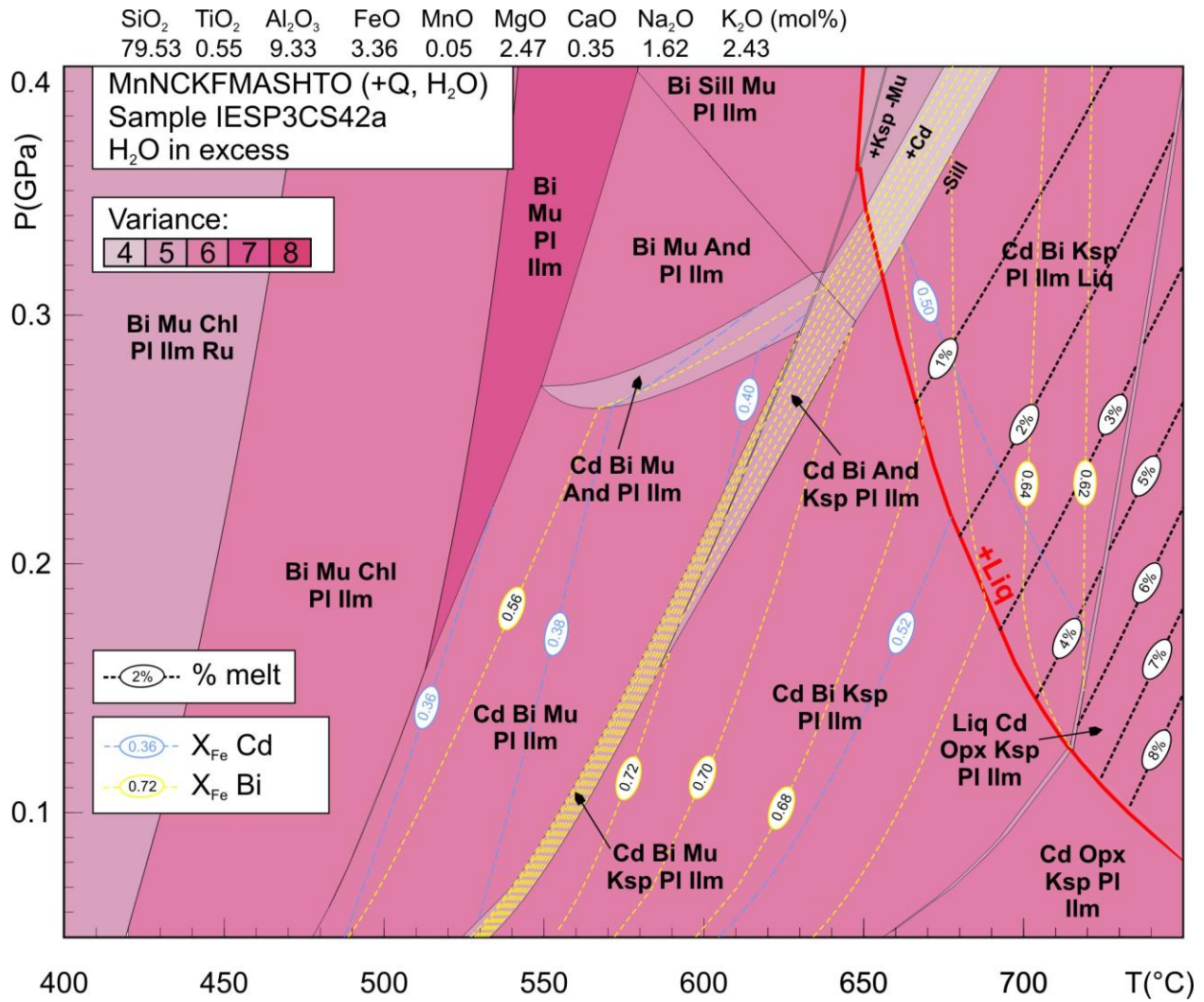
1284



1285

1286 Figure 12





1288 Figure 13

1289

1290

1291

**Table 1** – Radiometric ages in samples of metamorphic and igneous rocks from the Calamita peninsula, after a: Musumeci et al. (2011); b: Musumeci et al. (2015) and c: Viola et al. (2018). And = andalusite; Bi = biotite; Cd = cordierite; Di = diopside; Phl = phlogopite.

Rock type	Phase dated	Method	Age (Ma)
And-Cd-Bi schist	biotite	<sup>40</sup> Ar/ <sup>39</sup> Ar	6.23±0.06 Ma <sup>a</sup>
And-Cd-Bi schist	zircon	U/Pb	6.40±0.15 Ma <sup>a</sup>
Di-Phl marble	phlogopite	<sup>40</sup> Ar/ <sup>39</sup> Ar	6.76±0.08 Ma <sup>b</sup>

Leucogranite	white mica	$^{40}\text{Ar}/^{39}\text{Ar}$	$6.33\pm 0.07 \text{ Ma}^b$
Mylonite	authigenic illite	K/Ar	$6.14\pm 0.64 \text{ Ma}^c$
Fault gouge (CN-MAT)	authigenic illite	K/Ar	$4.90\pm 0.27 \text{ Ma}^c$

1292

1293

1294

1295

**Table 2** – Representative analyses of biotite, pinitized cordierite, K-feldspar, plagioclase, ilmenite and white mica in sample IESP3CS42A. T is the temperature estimated using the Ti-in-biotite geothermometer by Wu & Chen (2015). Ksp = K-feldspar. Ilm = ilmenite. Wm = white mica.

Analysis	Biotite							Cordierite		K-feldspar		Plagioclase		Ilm	Wm
	Resorbed				Euhedral, in		Retro	(pinitized)							Retro
	core	rim			Ksp										
	2	5	8	54	23	25	85a	1a	16a	22	48	46	102	83a	100a
SiO <sub>2</sub>	33.62	33.29	33.56	34.10	33.83	34.43	35.83	44.21	45.25	60.88	63.42	65.45	66.14	0.04	46.90
TiO <sub>2</sub>	2.02	2.10	3.19	2.90	1.84	1.85	0.83	0.04	0.00	0.00	0.00	0.04	0.00	50.79	0.14
Al <sub>2</sub> O <sub>3</sub>	18.50	18.16	17.51	18.29	18.35	18.70	16.87	29.57	29.98	17.42	18.30	21.14	22.55	0.00	31.54
FeO <sub>tot</sub>	23.34	23.40	22.23	23.01	22.13	20.83	18.98	6.47	7.77	1.61	0.24	0.41	0.04	40.31	1.82
MnO	0.07	0.13	0.04	0.05	0.06	0.05	0.06	0.00	0.00	0.00	0.00	0.00	0.01	3.89	0.02
MgO	6.80	6.79	6.92	6.78	7.02	7.38	10.81	3.44	3.54	1.14	0.14	0.00	0.00	0.03	1.23
CaO	0.02	0.02	0.00	0.05	0.01	0.08	0.00	0.09	0.00	0.04	0.05	2.50	3.31	0.06	0.04
BaO	0.11	0.04	0.09	0.12	0.06	0.10	0.00	0.13	0.02	0.71	0.87	0.00	0.00	0.00	0.11
Na <sub>2</sub> O	0.22	0.22	0.17	0.17	0.15	0.13	0.05	0.20	0.20	0.51	0.64	9.99	8.58	0.00	0.21
K <sub>2</sub> O	8.91	9.02	9.47	9.19	9.06	9.16	9.85	10.82	10.84	14.79	14.86	0.26	0.22	0.01	10.46
Total	93.61	93.17	93.17	94-66	92.50	92.72	93.27	94.97	97.59	97.09	98.52	99.78	100.8	96.99	92.48
Si	5.33	5.32	5.35	5.34	5.40	5.44	5.59	5.02	5.02	2.94	2.98	2.89	2.87	0.00	3.22
Al	3.46	3.42	3.29	3.38	3.45	3.52	3.10	3.96	3.92	0.99	1.01	1.10	1.15	0.00	2.56
Ti	0.24	0.25	0.38	0.34	0.22	0.22	0.10	0.00	0.00	0.00	0.00	0.00	0.00	1.01	0.01
Fe <sup>2+</sup> <sub>TOT</sub>	3.10	3.13	2.96	3.01	2.95	2.75	2.48	0.61	0.72	0.06	0.01	0.02	0.00	0.89	0.10
Mn	0.01	0.02	0.00	0.01	0.01	0.01	0.01	0.00	0.00	0.00	0.00	0.00	0.00	0.09	0.00
Mg	1.61	1.62	1.64	1.58	1.67	1.74	2.51	0.58	0.58	0.08	0.01	0.00	0.00	0.00	0.13
Ca	0.00	0.00	0.00	0.01	0.00	0.01	0.00	0.01	0.00	0.00	0.00	0.12	0.15	0.00	0.00
Ba	0.01	0.00	0.01	0.01	0.00	0.01	0.00	0.01	0.00	0.01	0.02	0.00	0.00	0.00	0.00
Na	0.07	0.07	0.05	0.05	0.05	0.04	0.02	0.04	0.04	0.05	0.06	0.85	0.72	0.00	0.03
K	1.80	1.84	1.93	1.84	1.85	1.85	1.96	1.57	1.53	0.91	0.89	0.01	0.01	0.00	0.92
T(°C)	591	594	650	644	575	573	423	-	-	-	-	-	-	-	-

1296

1297

1298

1299

1300